A preliminary evaluation of FY-4A visible radiance data assimilation by the WRF/DART-RTTOV system for a tropical storm case

Yongbo Zhou[1,2], Yubao Liu[1,2], Zhaoyang Huo[1,2], Yang Li[1,2]

[1]School of Atmospheric Physics, Nanjing University of Information Science and Technology, Nanjing, China

5   [2]Precision Regional Earth Modeling and Information Center (PREMIC), Nanjing University of Information Science and Technology, Nanjing, China

Correspondence to: Yongbo Zhou (yongbo.zhou@nuist.edu.cn)

Abstract. Satellite visible radiance data contain rich cloud and precipitation information that are increasingly assimilated for improving the forecasting skills of numerical weather prediction models. This study evaluates the Data Assimilation

10   Research Testbed (DART, Manhattan release v9.8.0), coupled with the Weather Research and Forecasting (WRF) model (ARW v4.1.1) and facilitated with an interface for the Radiative Transfer for TOVS (RTTOV, v12.3), for assimilating the simulated visible imagery of the FY-4A geostationary satellite located over Asia in a framework of Observing System Simulation Experiment (OSSE). The OSSE was performed for a tropical storm named Higos, which contains multi-layer and mixed-phase cloud structures and precipitation processes, to evaluate the advantages and limitations of the assimilation.

15   Single observation experiments and cycled DA experiments were performed to explore the pros and cons and sensitivities of the assimilation to different filter algorithms, cycling variables, outlier threshold values, and observation errors.

The assimilation significantly improved the first-guess forecast and analysis of cloud water path (CWP) and cloud coverage (CFC). After assimilating the visible radiances, WRF could capture better CWP and CFC properties for the Rank Histogram Filter (RHF) than the Ensemble adjustment Kalman Filter (EAKF) but with a sacrifice of more elapsed CPU time

20   ($\approx$ 7 min for EAKF and 13 min for RHF in one cycle), for the cycling variables including both cloud and non-cloud variables, for the larger outlier threshold values, and for the smaller observation errors without thinning of observations. The assimilation also generated slightly positive impacts on non-cloud variables due to feedback to the adjustments to cloud variables. In addition, the assimilation improved the representation of precipitation and rain rate. However, the improvements on rain rate are complicated by the inabilities of the assimilation to improve cloud vertical structures and

25   cloud phases. Sometimes, negative impacts could be introduced to cloud variables due to non-linear forward operator and non-Gaussian prior distribution. Future works should include the evaluation and development of faster and more accurate forward operators suitable for the assimilation of FY-4A visible imagery, techniques to reduce the non-linear and non-Gaussian errors, methods to correct the location errors, etc.

1. Introduction

All-sky satellite data assimilation (DA) has shown great potential to improve weather forecasts (Bauer et al., 2011). Most satellite DA-related studies deal with microwave (MW) and infrared (IR) data. DA of MW radiance data reveals positive effects on cloud and precipitation forecasting by adjusting the atmospheric state variables such as humidity and temperature (Geer et al., 2019; Migliorini and Candy, 2019) as well as cloud-related parameters such as cloud water/ice content and cloud coverage (Zhang et al., 2013; Yang et al., 2016). All-sky MW data has been operationally assimilated at some Numerical Weather Prediction (NWP) centres (Bauer et al., 2010; Zhu et al., 2016). However, operational DA of all-sky MW data is limited to humidity- and temperature-sounding channels (Carminati and Migliorini, 2021) because MW radiance at these channels is insensitive to surface emissivity and skin temperature, whose accurate estimates are challenging under cloudy skies (Hu et al., 2021). DA of MW data is also challenging to separate the radiance contribution from cloud and non-cloud variables (especially temperature and humidity) (Geer et al., 2017). The assimilation of all-sky IR radiance data also shows beneficial aspects. Existing studies suggest positive effects on water vapour and temperature by assimilating the IR data in clear sky (McCarty et al., 2009; Ma et al., 2017). In addition, DA of IR radiance data in cloudy regions shows improved analysis of column integrated water and improved forecasting skills in the mid- and upper-troposphere (Stengel et al., 2013; Geer et al., 2019). However, the assimilation of IR radiance data in cloudy regions is still complicated by the non-linear relationship between the observation and state variables and the related non-Gaussian problems (Li et al., 2022), the difficulty to separate cloud signals and non-cloud signals (Geer et al., 2017), and the difficulty to constrain the layered structures in multi-layer clouds (Prates et al., 2014).

To further improve cloud forecasts, there is great potential related to assimilating the visible (VIS) and shortwave infrared (collectively referred to as shortwave, SW) data (Vukicevic et al., 2004; Polkinghorne and Vukicevic, 2011; Scheck et al., 2020; Schröttle et al., 2020) because these measurements contain unique cloud information complementing the one contained in IR and MW data (Kostka et al., 2014; Schröttle et al., 2020). For example, SW radiation can penetrate a certain depth of cloud fields, and connotate cloud microphysical properties such as effective particle radius (Nakajima and King, 1990). In comparison, satellite IR data only provide information on cloud top microphysics (Xue, 2009). As a complement to precipitation radar that is much more sensitive to large hydrometeors or precipitation particles (Keat et al., 2019), which usually occurrs at the mature and developing stages of convective systems (Zhang and Fu, 2018), satellite SW radiance data are closely related to small cloud droplets. SW data usually have higher spatial resolution than MW data (Yang et al., 2017; Coste et al., 2017; Schimit et al., 2018). Therefore, high-resolution satellite SW radiance data provide information on cloud properties with great significance for cloud-resolving model simulation. Compared with the MW and IR data, the radiance contribution from cloud could be easily extracted from the VIS observations because the VIS radiance data is much more sensitive to cloud variables than non-cloud variables. In addition, VIS radiance is not sensitive to cloud layout in the vertical directions, but to the accumulated cloud properties. This makes the assimilation much easier for heterogeneous cloud scenarios. Therefore, assimilating the VIS radiance data has the potential to further improve the forecast quality of cloud and precipitation.

Many studies have attempted to assimilate the SW radiance data (direct assimilation) rather than the retrieved cloud parameters (indirect assimilation). Direct data assimilation critically depends on observation operators. Several observation operators and relevant algorithms have been developed for the assimilation of satellite VIS radiance data. For example, in the study of Vukicevic et al. (2004), model state variables were mapped to the equivalent radiance by an observation operator for the VIS and IR radiance measurements (VISIROO). Polkinghorne and Vukicevic (2011) used the Spherical Harmonic Discrete Ordinate Method Plane Parallel for Data Assimilation (SHDOMPPDA) for radiance conversion. SHDOMPPDA solves radiative transfer processes by Discrete Ordinate Method (DOM) in Cartesian space while computing source functions using spherical harmonic series in spherical space. Compared with observation operators which solve source functions in Cartesian space, SHDOMPPDA has the advantage of high computation efficiency. Scheck et al. (2016a) developed a Method for Fast Satellite Image Synthesis (MFASIS), which is 2 ~ 4 orders of magnitude faster than other observation operators based on DOM (Scheck et al., 2016b). Furthermore, a correction method was implemented in MFASIS to reduce errors due to three-dimensional (3D) radiative effects (Scheck et al., 2018). MFASIS is one of the observation operators of the Radiative Transfer for TOVS (RTTOV), which is a collection of observation operators widely used in satellite radiance DA (Saunders et al., 2018). Other radiative transfer solvers of the observation operators incorporated in the RTTOV package include DOM and the single-scattering method for SW radiative processes. These solvers could tackle cloud fraction, parallax correction, and many other critical aspects including molecular absorption and scattering, underlying surface reflection, etc. (Saunders et al., 2018). Apart from these aforementioned observation operators, some machine learning-based observation operators and relevant methods (Scheck, 2021; Zhou et al., 2021) were developed to achieve higher computation efficiency and accuracy for VIS radiance DA.

Another critical aspect of assimilating satellite VIS radiance data is the assimilation approach. There are two most commonly used approaches. The first is variational (VAR) methods. Vukicevic et al. (2004) assimilated GOES-9 VIS radiance data to the Regional Atmospheric Modeling System (RAMS) with a four-dimensional VAR (4DVAR) DA system, exhibiting positive effects on the short-term forecasting of a stratus cloud field. Similarly, Polkinghorne and Vukicevic (2011) assimilated the GOES-8 VIS and IR radiance data to RAMS by a 4DVAR system and indicated that the assimilation can effectively reduce the normalized cost function and the gradient of objective functions with the increase of iteration numbers. The second is ensemble-based methods. The ensemble-based methods are remarkably stable for nonlinear systems and are widely used for cloud- and precipitation-related studies (Lei et al., 2015; Kurzrock et al, 2019). Schröttle et al. (2020) assimilated VIS and IR radiance data in an idealized Observing System Simulation Experiment (OSSE) framework based on a Local Ensemble Transform Kalman Filter (LETKF). Their results indicated that assimilating VIS radiance data alone could improve the forecasting skills of the regional model termed Consortium for Small-scale Modeling (COSMO), and that assimilating the VIS and IR radiance data collaboratively could further improve the forecasting skills. Their findings were validated by Scheck et al. (2020). They concluded that assimilating the VIS radiance data of Spinning Enhanced Visible and Infrared Imager (SEVIRI) on METEOSAT could improve cloud and precipitation forecasts, and, meanwhile, the temperature and relative humidity forecasting errors were reduced in most conditions.

The VAR and ensemble-based approaches are considered complementary to each other. For example, the ensemble-based approaches generate the flow-dependent background error covariance matrices. On the other hand, the flow-dependence can be used to leverage the VAR approaches. Therefore, several hybrid approaches have been developed and great achievements have been made. Bauhner et al. (2013) evaluated an ensemble-variational DA approach in assimilating the observations which are operationally assimilated in Environment Canada, and concluded that the hybrid method is more skillful than variational methods to improve the short- and middle-range forecasting over tropical and extra-tropical regions. Gao et al. (2013) developed a hybrid Ensemble Kalman Filter (EnKF)-3DVAR method to effectively assimilate radar data. The hybrid EnKF-3DVAR method outperforms 3DVAR or EnKF in shortening the spin-up time of a supercell storm. In addition, the hybrid method is increasingly applied in satellite radiance DA. Xu et al. (2016) assimilated the FY-3B satellite MV radiance data by the WRF hybrid ensemble/3DVAR method, better forecasts of typhoons' track, intensities, and precipitation were reported compared with 3DVAR. Similar results were also reported by Shen et al. (2020).

Nowadays, there are various community DA resources of the ensemble-based methods, such as the Data Assimilation Research Testbed (DART, Anderson et al., 2009) which supports many numerical weather prediction models including the Weather Research and Forecasting (WRF) model (Skamarock et al., 2008). WRF/DART incorporated the RTTOV radiative transfer package, facilitating the assimilation of satellite radiance from VIS to MW wavelengths, enabling it with a great potential to assimilate all-sky satellite SW radiance data. The Advanced Geostationary Radiation Imager (AGRI) on the geostationary FY-4A satellite located over Asia excels at high sampling frequency (5 min for intensive observation and 15 min for usual observation) and high spatial resolution (0.5 ~ 2 km, depending on channels). Zhang et al. (2019) pointed out that AGRI has great application prospects in describing rapidly evolving and small- to medium-scale atmospheric systems. Since its launch in 2016, the FY-4A satellite provides abundant visible radiance data. However, these data are not currently assimilated in any of the operational numerical weather prediction centres.

Based on the analyses above, the simulated FY-4A/AGRI VIS radiance data were assimilated by the WRF/DART-RTTOV system in an OSSE framework to answer the following three questions. 1) What are the advantages and limitations of assimilating the FY-4A VIS radiance data to the forecast of a tropical storm case? 2) What are the better choices for the WRF-DART/RTTOV model settings and observation preparations? 3) What is the future work for the real DA applications of FY-4A VIS radiance data? The study is a preliminary evaluation of the WRF/DART-RTTOV system in assimilating all-sky FY-4A/AGRI VIS radiance data. The results should be representative of the upcoming FY-4B VIS radiance data because the designs of the AGRI payload for the two satellites are similar. The remaining manuscript is organized as follows. Models and experiment designs are introduced in Section 2. Impacts on the analysis and first-guess forecasts are discussed in Section 3. The conclusion of the study and related discussions are summarized in Section 4.

2. Models and experiment designs

The OSSE framework consists of a nature run, a control run, and several cycled DA experiments. A nature run was performed to generate a proxy true atmosphere. Several DA experiments by assimilating only the simulated VIS radiance

data were carried out to explore the impacts of the assimilation. A control run without DA was performed for comparison. The OSSE was performed based on a tropical storm case. On August 16, 2020, a tropical disturbance occurred over the north of Luzon, the Philippines. The system tracked northwest toward the South China Sea, and intensified into a tropical storm on 19:00 August 17. The tropical storm was further developed into a typhoon system named Higos on 12:00 UTC, August 18. The Higos landed on Zhuhai, Guangdong province on 22:00 UTC, August 18, and degenerated into a tropical depression on 12:00 UTC, August 19. This study focuses on the pre-landfall stage of the tropical storm (00:00 UTC ~ 12:00 UTC, August 18) under the consideration that FY-4A visible imagery is only available at daytime. The tropical storm has multi-layer and mixed-phase cloud structures, which facilitates the evaluation of the inabilities and ambiguities of assimilating visible radiance data for these cloud structures.

2.1 Configurations of the WRF Model

WRF model domain settings are the same for the nature run, the control run, and the cycled DA experiments to avoid errors due to displacement of grids between the observation and simulations. The WRF model domain for this study covers parts of the East Asia and Western Pacific (Figure 1). The domain contains 151×177 horizontal grid boxes with a grid spacing of 15 km in the horizontal directions and 40 vertical levels, with the model top set to 50 hPa. To avoid the disturbances over the regions close to the model domain boundaries, simulations within the inner rectangle of 131×157 horizontal grids are analysed.
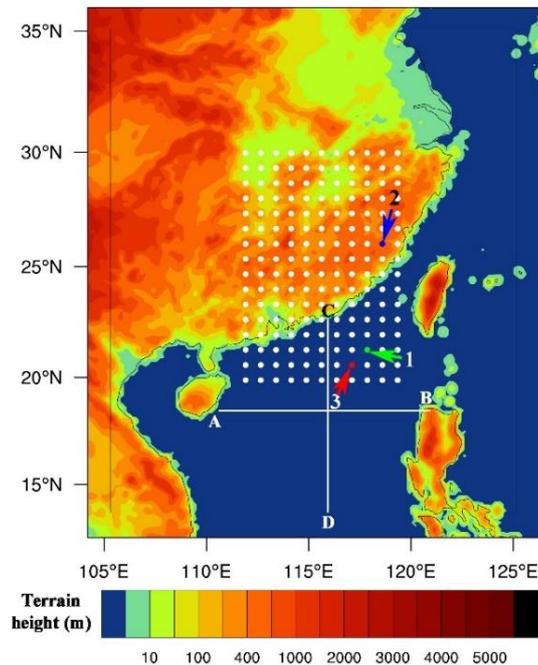
Figure 1. The WRF model domain with 15-km horizontal grid spacing. Only observations within the inner rectangle are assimilated to discard regions close to the model domain boundaries. The white dots denote the location where single observation experiments were discussed. Detailed discussions are given for points 1 (green), 2 (blue), and 3 (red). The two white lines including AB and CD are for cross-section analyses.

For the nature run, the initial conditions (ICs) and lateral boundary conditions (LBCs) were extracted from the National Centers for Environmental Prediction (NCEP) Final (FNL) Operational Global Analysis data ($1°\times1°$ resolution, available at https://rda.ucar.edu/datasets/ds083.2/). The WRF model configurations include the Thompson microphysical scheme (Thompson et al., 2008), the Tiedtke Cumulus Parameterization option (Tiedtke, 1989; Zhang et al., 2011), and the UV planetary boundary layer scheme (Bretherton and Park, 2009), which are the optimal schemes for typhoon simulations over the Northwest Pacific Ocean as suggested by Di et al (2019). Other model configurations include the revised MM5 Monin-Obukhov surface layer scheme (Jiménez et al., 2012), the five layer thermal diffusion land surface scheme (Dudhia, 1996), and the Rapid Radiative Transfer Model for Global Climate Models (RRTMG) longwave and shortwave radiation schemes (Iacono et al., 2008). With these model configurations, liquid water particles include cloud water droplets and rain drops, and ice particles include ice, snow, and graupel. The nature run was initialized by a cold start at 12:00 UTC 17 August, 2020. After a spin-up time of 14 hr, WRF model simulations between 02:00 ~ 12:00 UTC, 18 August, 2020 provided a proxy true atmosphere. The nature run could capture the bulk track properties which agree well with the observations. Synthetic observations were simulated by the RTTOV radiative transfer package detailed in Section 2.2. The simulated VIS imagery (15 km $\times$ 15 km resolution) was approximately equivalent to the superobbing of the 2km-resolution imagery, as provided by FY-4A real observations, by averaging the 2 km $\times$ 2 km imagery for every block of about 7$\times$7 pixels. Because the observation locations and model grid points are overlapped, the locations of the synthetic observations are directly assigned to the model grid points without interpolation during the assimilation processes.

For the cycled DA experiment, the ensemble size is set to 40 and the ICs and LBCs were extracted from the ERA5 hourly data ($0.25°\times0.25°$ resolution, available at https://cds.climate.copernicus.eu/api/v2). Perturbations extracted from the WRF 3DVAR system using a generic background error option which draws the NCEP background error covariances with proper scaling were added to the ICs. The scaling factors for the variance, horizontal length scale, and vertical length scale are set to 0.25, 1.0, and 1.5, respectively. To avoid discontinuities and poor results at the boundary, LBCs at each analysis time were updated based on the analysis and WRF lateral boundary conditions by an approach built in the DART *pert_wrf_bc* module. This is the reason why we choose the higher resolved LBCs, as we will do in real DA applications, for the DA experiments than for the nature run. The WRF model microphysics configurations are the same as the nature run. The first-guess forecasts of the ensemble members were initialized by a cold start at 00:00 UTC 18 August, 2020. After a spin-up time of 2 hr, synthetic visible radiance observations were assimilated to the ensemble members from 02:00 to 09:00 UTC 18 August, 2020. The time span corresponds to the daytime when VIS imagery is available. After 09:00 UTC, the ensemble members were advanced until 12:00 UTC. The updating frequency of the first-guess state variables was set according to different experiment designs summarized in Table 1. By these set ups, the effects of assimilating VIS imagery on shortening the spin-up time of WRF model, and on the analysis and the first-guess forecast of state variables, cloud and precipitation were explored. The model settings for the control run are the same as the cycled DA experiments, except that no observations were assimilated.

2.2 Configurations of RTTOV

Synthetic AGRI channel 2 radiance was simulated by the RTTOV radiative transfer package based on WRF state variables. The input parameters of RTTOV include cloud-related parameters (the vertical structures of the mixing ratio of liquid water mixing ratio, ice water mixing ratio, cloud water effective radius, cloud fraction, etc.), atmosphere profiles (the water vapour mixing ratio profile, temperature profile, etc.), surface properties (elevation, surface type, etc.), sun-satellite viewing geometries, etc. In partly cloudy regions, the TOA radiance is a weighted average of the radiance for a clear sky and a cloudy sky. For an independent column, the weight (effective cloud fraction) was calculated by a hydrometeor weighted average across the vertical profile of input cloud fraction (Geer et al., 2009). It is noted that cloud fraction (CFC) parameterization in WRF model depends on relative humidity (RH), the saturation water vapour mixing ratio (q^*), and cloud water + ice mixing ratios (q_{l+i}) (Xu and Randall, 1996),

$$\text{CFC} = \begin{cases} RH^p \left[1 - \exp\left(\frac{-\alpha q_{l+i}}{[(1-RH)q^*]^\gamma}\right)\right], if\ RH < 1 \\ 1, if\ RH \geq 1 \end{cases} \tag{1}$$

where p, α, and γ are suggested to be 0.25, 100, and 0.49 separately.

The solar zenith angle, solar azimuth angle, satellite viewing zenith angle, and satellite azimuth angle were calculated by the Python astropy library based on the UTC time and the FY-4A satellite position (104.7 °E at the geostationary satellite orbit). In addition, observation errors ranging from $1 \sim 4$ mW m^{-2} sr^{-1} were assigned to the observations (Table 1). RTTOV includes the pre-defined cloud optical properties. For liquid water clouds, we use the "Deff" scheme where cloud optical properties are parameterized in terms of Re (Mayer and Kylling, 2005). The cirrus scheme developed by Baren et al. (2014) was used to calculate ice cloud optical properties, which has no explicit dependence on ice particle size. Therefore, analyses of the results were simplified given that cloud variables were adjusted collectively but we do not have to analyse the effective radius of ice particles.

The radiative transfer processes are simulated by the DOM solver in RTTOV. The surface was treated as a specular reflector for downwelling emitted radiance. For land surface, the surface Bidirectional Reflectance Distribution Function (BRDF) was drawn from land surface atlases (Vidot and Borbás, 2014; Vidot et al., 2018). For sea surface, BRDF was calculated by the JONSWAP (Hasselmann et al., 1973) solar sea BRDF model. The lay-to-space transmittance was computed by the v9 predictor on 54 levels (Matricardi, 2008). The downwelling atmospheric emission was computed using the linear-in-tau approximation for the Planck source term. Water vapour profiles were drawn from WRF state variables. Other parameters not explicitly mentioned are set to default values.

Based on the above model configurations, the dependence of AGRI channel 2 radiance on the Cloud Water Path (CWP) and effective radius of cloud water droplet (Re) is presented in Figure 2, where CWP denotes the vertically integrated cloud liquid and ice water mixing ratio in an atmospheric column, which is calculated by the formula,

$$\text{CWP} = \int_{P_s}^{P_t} \frac{1}{g}(Q_c + Q_i)dP \tag{2}$$

where P_s and P_t denote surface and at the model top pressure. Qc and Qi are the liquid water mixing ratio (the sum of the mixing ratio of cloud droplet and rain) and ice water mixing ratio (the sum of the mixing ratio of ice, snow, and graupel), and g the gravitational acceleration (9.8 ms^{-2}).
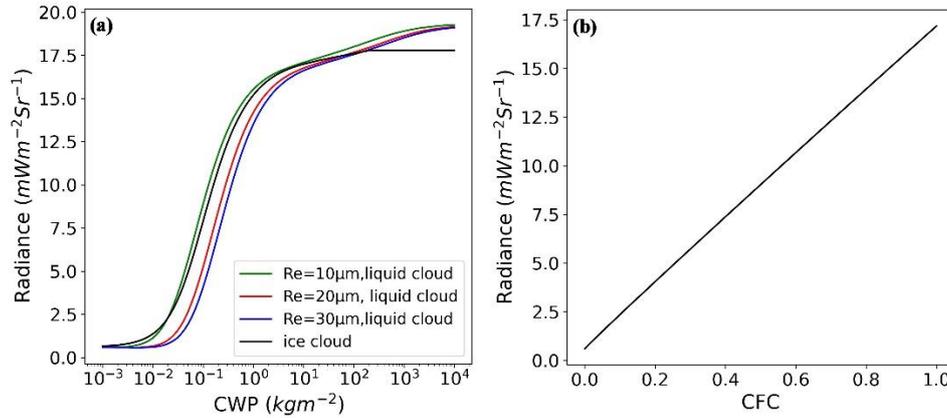
Figure 2. (a) Dependence of AGRI channel 2 radiance on cloud water path (CWP) and effective radius (Re). (b) Dependence of AGRI channel 2 radiance on cloud fraction (CFC) for CWP of 10 kg m^{-2} and Re of 15 µm. The simulation is performed with the "Deff" scheme for liquid water cloud optical properties and the Baren et al. (2014) scheme for cirrus optical properties. The solar zenith angle, viewing zenith angle, and relative azimuth angle are 25°, 40°, and 135°, respectively.

The curvature properties clearly show a non-linear relationship between the observations (radiance) and cloud related parameters (CWP and Re). The differences between the radiance-CWP functions with different effective radii become smaller as Re increases. For Re larger than 30 µm, the radiance-CWP functions for different effective radii are ignorable. Because raindrops are several orders larger than cloud droplets, the effective radius of cloud droplets is sufficient to describe the radiative transfer processes for the clouds where cloud droplets and raindrops coexist. As a result, Re in the following discussion explicitly denotes the effective radius of cloud droplets, which corresponds to the WRF state variable "RE_CLOUD".

2.3 DA experiment design and DART configurations

2.3.1 DART filters

DART was configured to employ the Ensemble Adjustment Kalman Filter (EAKF, Anderson, 2001) and the Rank Histogram Filter (RHF, Anderson, 2010). EAKF and RHF are two variants of the deterministic filters. Therefore, no perturbations were added to the observations. EAKF is a serial ensemble DA algorithm and the observations are assimilated as scalars. The model state variable x_m is updated by Equation (3) (Anderson, 2001),

$$x'_m = x_m + \Delta \mathbf{x}_{m,n}, \qquad m = 1, \dots, M, n = 1, \dots, N \tag{3}$$

where x_m denotes the mth state variable, x'_m the updated value of x_m, and $\Delta x_{m,n}$ the state variable increment for the mth state variable due to the nth observation. $\Delta x_{m,n}$ is calculated by Equation (4),

$$\Delta x_{m,n} = (\sigma_{p,m}/\sigma_p^2)\Delta y_n, \qquad m = 1, \dots, M, n = 1, \dots, N \tag{4}$$

where the subscript "p" is the abbreviation of "prior", $\sigma_{p,m}$ is the prior sample covariance between the observation and the mth state variable x_m, and σ_p^2 the prior sample variance of the observed variable. Δy_n is the observation increment for the nth observation, which is calculated by the following equation,

$$\Delta y_n = (y_n^p - \bar{y}_p)(\sigma_u/\sigma_p) + \bar{y}_u - y_n^p, \qquad n = 1, \dots, N \tag{5}$$

where y_n^p denotes the nth prior observation, $\bar{y}_p$ the prior ensemble mean observation, $\bar{y}_u$ the posterior ensemble mean observation, σ_u the updated standard deviation of σ_p. $\bar{y}_u$ and σ_u are calculated by Equations (6) ~ (7).

$$\overline{y_u} = \frac{\sigma_o^2}{\sigma_o^2+\sigma_p^2}\bar{y}_p + \frac{\sigma_p^2}{\sigma_o^2+\sigma_p^2}y_o \tag{6}$$

$$\sigma_u = \frac{\sigma_o\sigma_p}{\sqrt{\sigma_o^2+\sigma_p^2}} \tag{7}$$

where y_o and σ_o denote the observation and its corresponding observational error standard deviation.

Anderson (2007; 2009) promoted a spatially varying state-space adaptive covariance inflation to the prior state to increase prior ensemble spread. The same option is adopted in this study and other papers (Lei et al., 2015; Kurzrock et al., 2019). The adaptive inflation uses 1.0, 0.6, and 0.9 as the initial value, fixed standard deviation, and damping settings, respectively. The sampling error due to the use of the limited ensemble size was corrected by the method developed by Anderson (2012). Since bulk-layer observations like satellite VIS radiance data do not have a specific single vertical location, no vertical localization was used in this study.

The RHF produces a posterior ensemble based on a continuous approximation of the prior Probability Density Function (PDF) and a piecewise linear representation of the likelihood. The prior PDF is approximated by a rank histogram which has a piecewise constant between two ensemble members and follows Gaussian distributions beyond the lower and upper bounds of the ensemble members. The posterior distribution is calculated by the Bayes Theorem, and the state variable is updated by searching the appropriate position in the state variable space which partitions the posterior distribution to unity probability for each ensemble member. The prior PDF does not have to respect the Gaussian form for RHF. Therefore, the method is declared to be more suitable for non-Gaussian problems. Details on this algorithm are elaborated in Anderson (2010).

2.3.2 Single observation experiments

With the OSSE set ups configured with EAKF, a set of single observation experiments were performed. The single observation experiments assimilate an observation at a targeting pixel, and the adjustment of state variables at the targeting

pixel is only caused by the assimilation of one observation. Therefore, it is convenient to demonstrate the basic technical functionality of assimilating visible radiance data by employing EAKF by single observation experiments. The potentials, inabilities and ambiguities of assimilating VIS radiance data were discussed in this section. The single observation experiments were performed at 02:00 UTC 18 August, 2020, and forecasts were not carried out. The focusing cloud variables include Qc, Qi, Re, and CFC. The focusing non-cloud variables include water vapour mixing ratio (QVAPOR), perturbation potential temperature (T), and the x- and y-wind components (U and V).

270

The single observation experiments were performed for the most inner parts of the satellite imagery to avoid disturbances near boundaries. The observations at 02:00 UTC were thinned by selecting every six pixels to make sure that the selected observations are far from each other. This will generate 176 points shown in Figure 1. By setting a localization distance of 15 km, assimilating the visible radiance at a pixel would not influence the state variables at surrounding pixels. Therefore, we performed the 176 single observation experiments in one DA cycle to save computational cost as performed by Scheck et al. (2020). Amongst the 176 selected pixels, special focuses were given to the three coloured points, which were designed to illustrate the ambiguities related to cloud layered structures and cloud phases and to illustrate the inabilities related to the non-Gaussian and non-linear problems.

275

2.3.3 Cycled DA experiments

280

In an OSSE framework, fourteen cycled DA experiments were performed to evaluate the influences of different model settings and observation preparations on the analysis and the first-guess forecast when VIS radiance data was assimilated. The purpose of the cycled DA experiments is to reveal the forecast quality and growth of the forecasting errors by assimilating satellite VIS radiance data, and to provide some guidance on the settings of WRF/DART-RTTOV and an outlook to the future works. The experiment set ups cover different filter algorithms, cycling intervals, cycling variables, outlier threshold values, observation errors, and observations with or without thinning. The outlier threshold value is a pre-defined threshold value for rejecting an observation depending on its distance from the prior ensemble mean. If the distance is more than N (the predefined outlier threshold value) standard deviations from the square root of the sum of the prior ensemble and observation error variance, the observation is rejected. The experiment designs are summarized in table 1.

285

Comparison between Exp-01 ~ Exp-03 and Exp-4~Exp-06 experiment group was designed to reveal the pros and cons of EAKF and RHF for the analysis and first-guess forecast. Comparison between Exp-01 ~ Exp-02 and Exp-07 ~ Exp-08 experiment group was designed to reveal the influences of updating the thermal and dynamic variables on the analysis and first-guess forecast. Comparison between Exp-03, Exp-09, and Exp-10 was designed to reveal the influences of observation error on the analysis and first-guess forecast. Comparison between Exp-01 ~ Exp-03 and Exp-11~ Exp-13 experiment group was designed to reveal the influences of the outlier threshold value on the analysis and first-guess forecast. Comparison between Exp-10 and Exp-14 was designed to reveal the influences of observation thinning on the analysis and first-guess forecast.

290

295

Table 1. Parameter settings for the cycled data assimilation experiments. x_{cloud} denotes the WRF cloud variables including cloud fraction (CLDFRA), the mixing ratio of cloud droplet (QCLOUD), rain (QRAIN), ice (QICE), snow (QSNOW), graupel (QGRAUP), the effective radius of cloud water droplet (RE_CLOUD), and the effective radius of cloud ice droplet (RE_ICE). x_{atmos} denotes the WRF non-cloud variables including water vapour mixing ratio (QVAPOR), water vapour mixing ratio at 2m height (Q2), the x-, y-, and z-wind components (U, V, W), the x- and y-wind components at 10 m height (U10 and V10), temperature at 2 m height (T2), the perturbation geopotential (PH), the perturbation potential temperature (T), the perturbation dry air mass in column (MU), and the surface pressure (PSFC).

DA experiments	Thinning length	Localization distance	Filter algorithm	Cycling interval	Cycling variables	Outlier threshold	Observation error
Exp-01	——	15 km	EAKF	10 min	$x_{cloud}+x_{atmos}$	3	1 mW m^{-2} Sr^{-1}
Exp-02	——	15 km	EAKF	1 hr	$x_{cloud}+x_{atmos}$	3	1 mW m^{-2} Sr^{-1}
Exp-03	——	15 km	EAKF	3 hr	$x_{cloud}+x_{atmos}$	3	1 mW m^{-2} Sr^{-1}
Exp-04	——	15 km	RHF	10 min	$x_{cloud}+x_{atmos}$	3	1 mW m^{-2} Sr^{-1}
Exp-05	——	15 km	RHF	1 hr	$x_{cloud}+x_{atmos}$	3	1 mW m^{-2} Sr^{-1}
Exp-06	——	15 km	RHF	3 hr	$x_{cloud}+x_{atmos}$	3	1 mW m^{-2} Sr^{-1}
Exp-07	——	15 km	EAKF	10 min	x_{cloud}	3	1 mW m^{-2} Sr^{-1}
Exp-08	——	15 km	EAKF	1 hr	x_{cloud}	3	1 mW m^{-2} Sr^{-1}
Exp-09	——	15 km	EAKF	3 hr	$x_{cloud}+x_{atmos}$	3	2 mW m^{-2} Sr^{-1}
Exp-10	——	15 km	EAKF	3 hr	$x_{cloud}+x_{atmos}$	3	4 mW m^{-2} Sr^{-1}
Exp-11	——	15 km	EAKF	10 min	$x_{cloud}+x_{atmos}$	6	1 mW m^{-2} Sr^{-1}
Exp-12	——	15 km	EAKF	1 hr	$x_{cloud}+x_{atmos}$	6	1 mW m^{-2} Sr^{-1}
Exp-13	——	15 km	EAKF	3 hr	$x_{cloud}+x_{atmos}$	6	1 mW m^{-2} Sr^{-1}
Exp-14	60 km	60 km	EAKF	3 hr	$x_{cloud}+x_{atmos}$	3	1 mW m^{-2} Sr^{-1}

2.4 Metrics of simulation errors

The Root Mean Square Error (RMSE) and Mean Absolute Error (MAE) are two of the most commonly used metrics to assess the simulation errors (Kurzrock et al., 2019). Compared with MAE, RMSE is much more sensitive to extremely large errors. For satellite VIS radiance assimilation, extremely large analysis increments of CWP were rarely expected (details provided in Section 3), implying that the difference of RMSE between the first-guess and the analysis was not as distinct as MAE. In order to demonstrate the influences of assimilating the VIS radiance data more clearly, MAE is used to measure the difference between the simulated CWP and the theoretical true CWP (derived from the nature run). MAE is calculated by the following formula,

$$\text{MAE} = \frac{1}{n_x n_y} \sum_{i,j} abs(x_{i,j}^{\text{sim}} - x_{i,j}^{obs}) \tag{8}$$

where $x_{i,j}^{\text{sim}}$ ($x_{i,j}^{obs}$) denotes the simulated (true) CWP at the ith (in the zonal direction) and j[th] (in the meridional direction) model grid. n_x and n_y denote the number of pixels in zonal and meridional directions of the relevant model domains.

The fraction skill score (FSS) is used to measure cloud location errors in the horizontal directions for the cycled DA experiments, which is defined as,

$$FSS = 1 - \frac{\frac{1}{m_x m_y} \Sigma_{i,j} \left(p_{i,j}^{obs} - p_{i,j}^{sim} \right)^2}{\frac{1}{m_x m_y} \left[\Sigma_{i,j} p_{i,j}^{obs} + \Sigma_{i,j} p_{i,j}^{sim} \right]} \qquad (9)$$

where $p_{i,j}^{obs}$ denotes the cloud fraction within a subdomain covering 3×3 model grids. m_x and m_y denote the number of subdomains in the zonal and meridional directions.

For the evaluation of precipitation simulations, the Threat Score (TS) is used to assess the representation of precipitation,

$$TS = \frac{H}{F + M + H} \qquad (10)$$

where H denotes the number of pixels with the correct representation of precipitation (hits), F denotes the number of pixels where simulation indicates precipitation while the true state indicates non-precipitation (false alarms), and M denotes the number of pixels where simulation indicates non-precipitation while the true state indicates precipitation (under predictions).

Following Scheck et al. (2020), we use the Mean Profile Error (MPE, denoted as ε) to assess the error of model state with respect to the nature run. If the difference of MPE between the posterior and the prior estimates ($\delta\varepsilon = \varepsilon_{pos} - \varepsilon_{pri}$) is negative, a positive impact was generated by the assimilation procedure, and vice versa.

3. Results

3.1 Single observation experiments

The results in this section correspond to the OSSE set ups elaborated in Section 2.3.2. Only the first guess and the analysis state variables were analysed here, including three cases. 1) The posterior is within the range bounded by the prior estimate and the truth both in the state variable and observation spaces. 2) The posterior is within the prior estimate and the truth in observation space but not in state variable space, which is closely related to the spurious covariance and the non-linear properties of the forward operator. 3) The posterior is beyond the prior estimate and the truth both in observation space and in state variable space, which is closely related to the non-Gaussian properties of the prior PDF. The results including the three cases are shown in Figure 3.

Assimilating VIS radiance data generated neutral impacts on the non-cloud variables including x- and y-wind components (U and V in Figure 3(a)), temperature and water vapour mixing ratio (T and Q in Figure 3(b)). From the perspective of radiative transfer processes, the VIS radiance is insensitive to U and V at the analysis time. Therefore, the adjustment in observation space should not generate beneficial impacts on U and V. In addition, VIS radiance is closely related to CFC (Figure 2(b)), an implicit relationship between VIS radiance and RH should be expected due to the parameterization of CFC due to Equation (1). In addition, VIS radiance data are positively related to CFC. Given that RH

not only depends on Q, but also on T and pressure, spurious covariance between VIS radiance and Q/T was generated due to the ensemble spread of Q/T (different Q/T for the ensemble members would blur the relationship between VIS radiance and Q/T). Therefore, neutral impacts on Q and T were revealed for the single observation experiments. Because RH is not a state variable for WRF model, the results on RH were not presented explicitly.
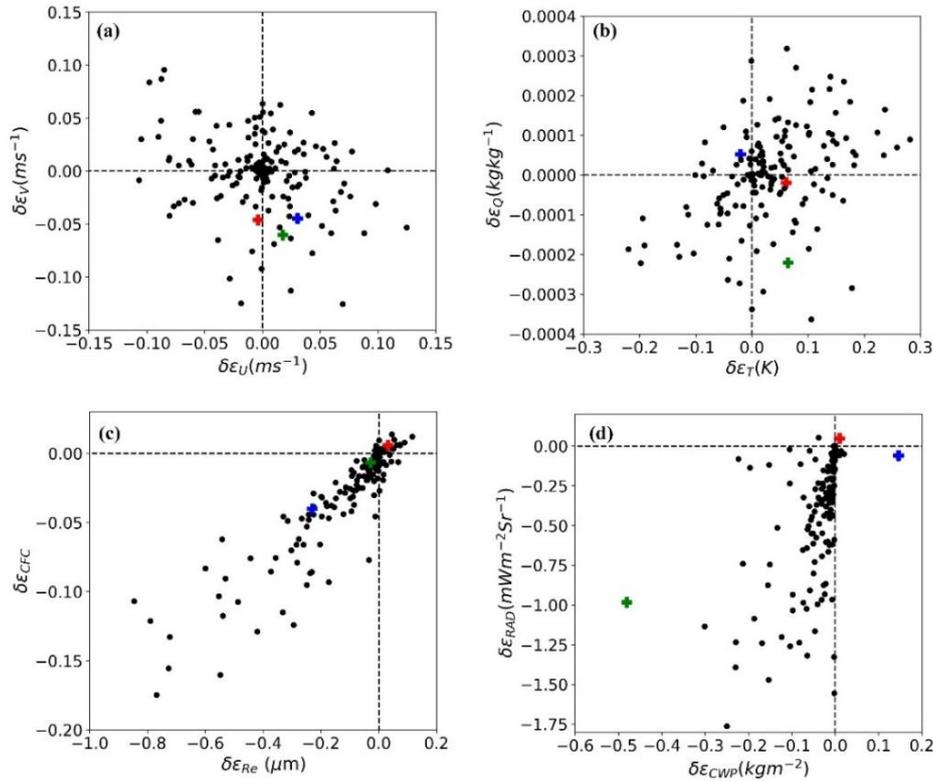
350

Figure 3. Differences of the mean profile errors between the prior and posterior estimates, denoted as $\delta\varepsilon_X = X_{MPE,pos} - X_{MPE,pri}$, where X denotes a state variable or a diagnosed parameter, and pos and pri the posterior and prior estimates. The variables include the x- and y-wind components (U and V), perturbation potential temperature (T), water vapour mixing ratio (Q), cloud fraction (CFC), cloud water path (CWP), and radiance. The plus signs in green, blue, and red colours correspond to points 1, 2,
355   and 3 in Figure 1.

Assimilating VIS radiance data generated positive impacts on Re, CFC, CWP, and in the observation space for most of the points (Figure 3(c) and 3(d)). Take the point 1 in Figure 1 as an example of case 1, the profiles of cloud and non-cloud variables for the first guess and analysis are shown in Figure 4. Point 1 corresponds to a one-layer ice cloud between 400 ~ 200 hPa with a CWP of 0.01 kg m^{-2} and a top-of-atmosphere (TOA) radiance of 3.63 mW m^{-2} Sr^{-1} for the nature run. The

360   first-guess forecast simulated a two-layer mixed-phase cloud with a false alarm liquid water cloud simulated below 500 hPa. The first-guess ensemble mean CWP and the equivalent VIS radiance are 1.33 kg m^{-2} and 7.29 mW m^{-2} Sr^{-1}, respectively. After assimilating the satellite VIS radiance data, the first guess was drawn toward the nature run both in the observation space, with a decreased ensemble mean radiance of 6.40 mW m^{-2} Sr^{-1}, and in the CWP space, with a decreased ensemble

mean CWP of 0.85 kg m⁻². As a result, Qc, Qi, CFC, and Re were adjusted collaboratively toward the nature run. Since model settings of RTTOV have no explicit dependence on the effective radius of ice particles, the adjustment of this variable is not discussed explicitly.
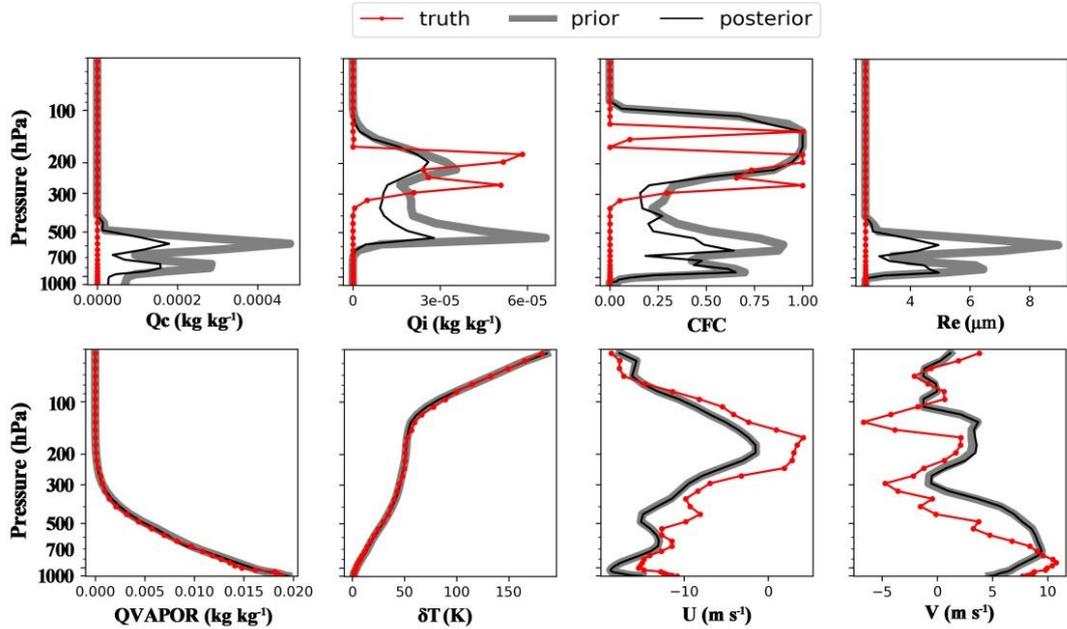
Figure 4. The vertical profiles of state variables for the nature run (theoretical truth), the prior and posterior estimates of sate variables. Qc denotes the liquid water mixing ratio, Qi the ice water mixing ratio, CFC the cloud fraction, Re the effective radius of liquid water droplets, QVAPOR the water vapour mixing ratio, δT the perturbation potential temperature, U and V the x- and y-wind components.

The synthetic VIS radiance observation is not sensitive to cloud vertical structures but to the accumulated cloud water/ice mass. As a result, it is difficult to correct cloud vertical location errors due to a lack of information on cloud top height and vertical cloud extent. In addition, the assimilation cannot remove the false alarm liquid clouds due to the spurious covariance between the VIS radiances and liquid water clouds in the background. According to formula (4), the analysis increment of each state variable is linearly related to its covariance with observation. Therefore, the vertical structures and phases of the posterior estimate are mainly determined by those of the prior estimate. A larger first-guess estimate of the state variable would generate larger covariance, and a larger adjustment of the first guess should be expected. Because the first-guess Qc and Qi were larger in the lower layer (≥ 400 hPa), the adjustment of Qc/Qi were much more distinct for the lower layer than the upper layer (≤ 300 hPa). Similar results were also found for Re except that larger liquid water particles occurred in the middle layer (~ 600 hPa) and smaller liquid water particles occurred in the lower layer (~ 800 hPa). The covariance between CFC and synthetic observation is zero in the upper layer (≤ 200 hPa) because CFC is almost a constant of 1 for all ensemble members (the ensemble spread of CFC is zero). Compared with the cloud variables, the non-cloud variables remain almost unchanged after assimilating the synthetic VIS radiance data.

385   For case 2, a positive impact in observation space does not ensure a positive impact in CWP space. Take the point 2 in Figure 1 as an example, the first-guess ensemble mean, posterior ensemble mean, and the observation of VIS radiance (CWP) are 7.94 mW m^{-2} Sr^{-1} (2.50 kg m^{-2}), 8.00 mW m^{-2} Sr^{-1} (2.65 kg m^{-2}), and 8.59 mW m^{-2} Sr^{-1} (0.17 kg m^{-2}), respectively. This is partly caused by the non-linear relationship between model state variables and visible radiance. To illustrate this problem specifically, calculating the ensemble mean of formula (4) and substituting $\overline{y_u}$ with formula (6) would get the following

390   formula,

$$\overline{\Delta x_m} = \frac{\sigma_{p,m}}{\sigma_o^2 + \sigma_p^2} R_{inc} \tag{11}$$

where Δx_m denotes the ensemble mean of the mth state variable increment, R_{inc} the ensemble mean radiance increment, which is calculated by the following formula,

$$R_{inc} = y_o - \bar{y}_p \tag{12}$$

395   Considering a simplified case with 2 ensemble members, the ensemble mean observation increment is calculated by the following formula,

$$R_{inc} = F(W_o) - \frac{F(W_1) + F(W_2)}{2} \tag{13}$$

where F denotes the forward operator. W_1 and W_2 represent CWP of the two ensemble members. However, considering the relationship between CWP and the VIS radiance, the theoretical true observation increment should be,

400 $$R_{inc}^t = F(W_o) - F(\overline{W}), \overline{W} = \frac{W_1 + W_2}{2} \tag{14}$$

    As indicated by Figure 4, R_{inc} is larger than R_{inc}^t. Namely, the ensemble mean observation increment was overestimated by Equation (14), leading to an over-estimated posterior ensemble mean CWP.

    For case 3, negative impacts could be even generated in the observation space. Take the point 3 in Figure 1 as an example, the posterior ensemble mean observation (2.51 mW m^{-2} Sr^{-1}) is beyond the range bounded by the first-guess

405 ensemble mean (2.56 mW m^{-2} Sr^{-1}) and the theoretical true observation (3.41 mW m^{-2} Sr^{-1}). The EAKF algorithm assumes that the prior PDF, denoted as $p(x)$, of model state variables (or the diagnosed variable such as CWP in this study) confirms to a Gaussian function. To see how well the assumption was respected, $p(x)$ in the CWP space is presented in Figure 6, which indicates a non-Gaussian prior PDF in CWP space. Several studies concluded that the non-Gaussian properties affect the performance of ensemble methods negatively (Lawson & Hansen, 2004; Lei et al., 2010). Therefore, we ascribe the

410 negative impacts in the observation space partly to the non-Gaussian properties of $p(x)$. Accordingly, a DA experiment using the RHF was added in comparison with EAKF.
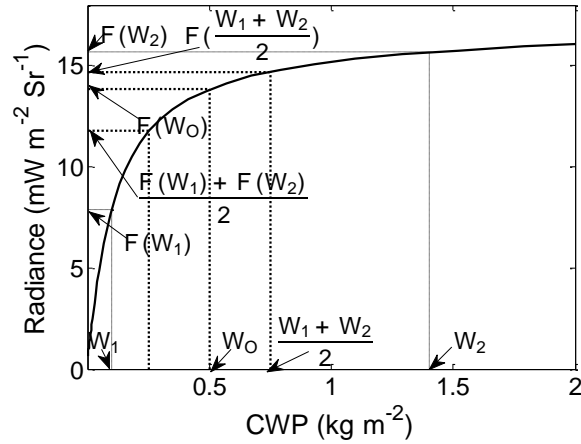
Figure 5. Illustration of the effects of nonlinearity of the observation operator on the calculation of radiance increments with 2 ensemble members. F denotes the observation operator, W_1 and W_2 denote cloud water path (CWP) for the 1st and 2nd ensemble member, W_O denotes the observed CWP. R_{inc} denotes the calculated ensemble mean radiance increment, and R_{inc}^t denotes the true radiance increment which respects the laws between the CWP and the radiance.
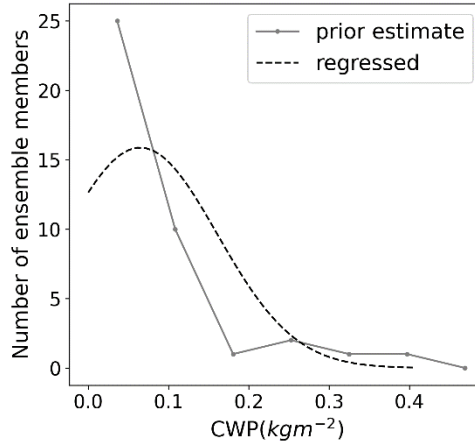
Figure 6. The first-guess probability density function in cloud water path (CWP) space, which is estimated from the 40 prior ensembles, for the point 3 (red dot) in Figure 1.

3.2 Cycled DA experiments

The results in this section correspond to the OSSE set ups elaborated in Section 2.3.3. The main focuses are the impacts of assimilation on the analysis and first-guess forecast of CWP, cloud coverage, non-cloud state variables, and precipitation.

3.2.1 Impacts on CWP and cloud coverage

The time evolution of CWP for the nature run, control run, and the first-guess forecast and the analysis of CWP for Exp-01 are presented in Figure 7.
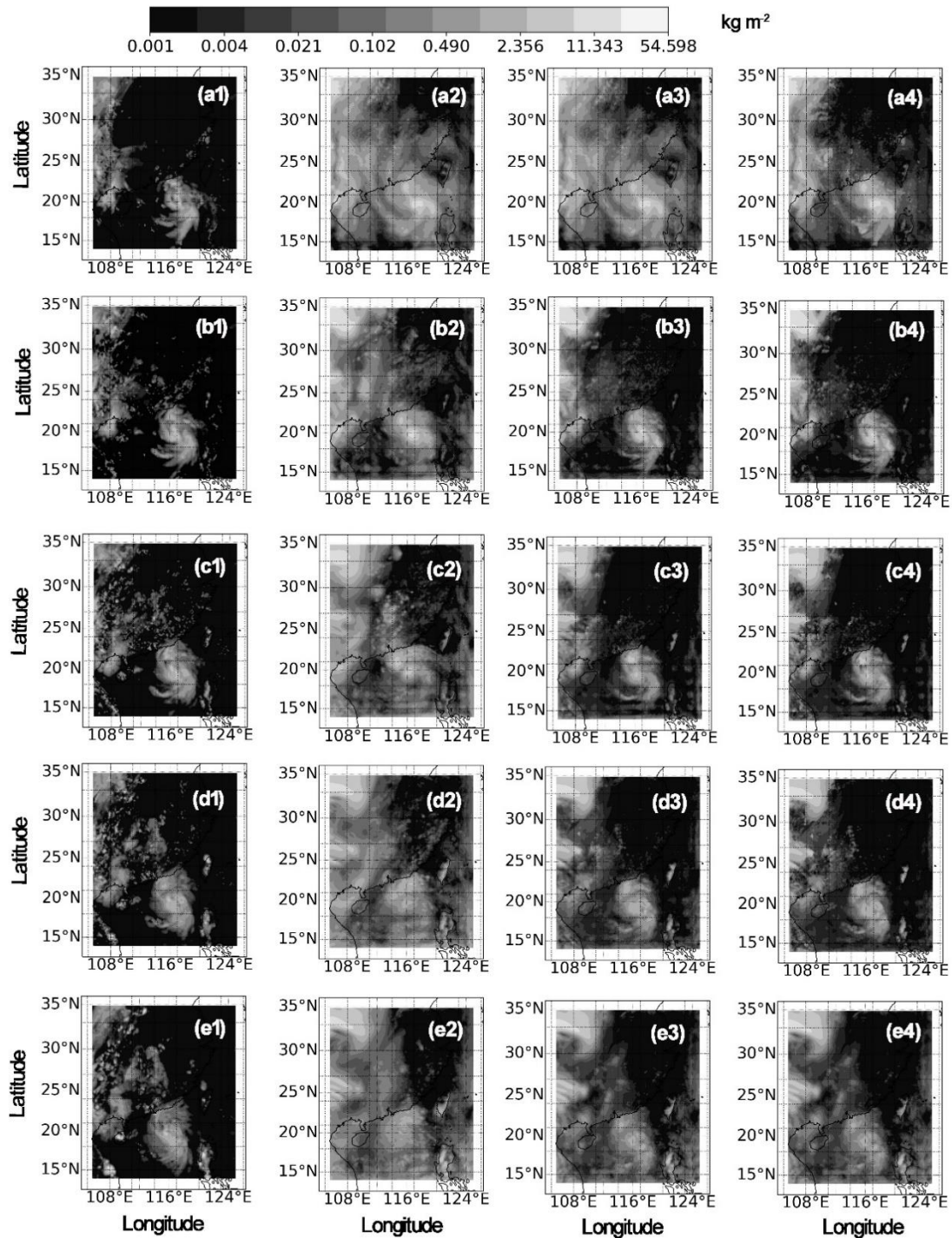
Figure 7. The time evolution of cloud water path (CWP) for the nature run (column 1), the control run (column 2), the first-guess forecast (column 3) and analysis (column 4) of Exp-01. From top to bottom, the row panels correspond to 02:00, 04:00, 06:00, 08:00, and 10:00 UTC on 18 August 2020.

430 The results indicate distinct differences between the first guess and the analysis of CWP at the first analysis time (02:00 UTC, 18 August, 2020). After the first analysis time, the horizontal distribution of CWP of the first guess is quite similar to the analysis. Namely, an extremely large analysis increment of CWP was rarely expected as indicated by 2.4. This validates the reason why we chose MAE rather than RMSE to verify the prior and posterior estimates. The resemblance between the cycled DA experiments and the nature run also indicates the improvements on the analysis and the first-guess forecast of
435 CWP and cloud coverage. Compared with the control run, assimilating VIS radiance data could clearly suppress the false alarm clouds. However, the assimilation could not generate clouds which are under-predicted. The inability to correct the underprediction was illustrated by a cross-section analysis shown in Figure 8.
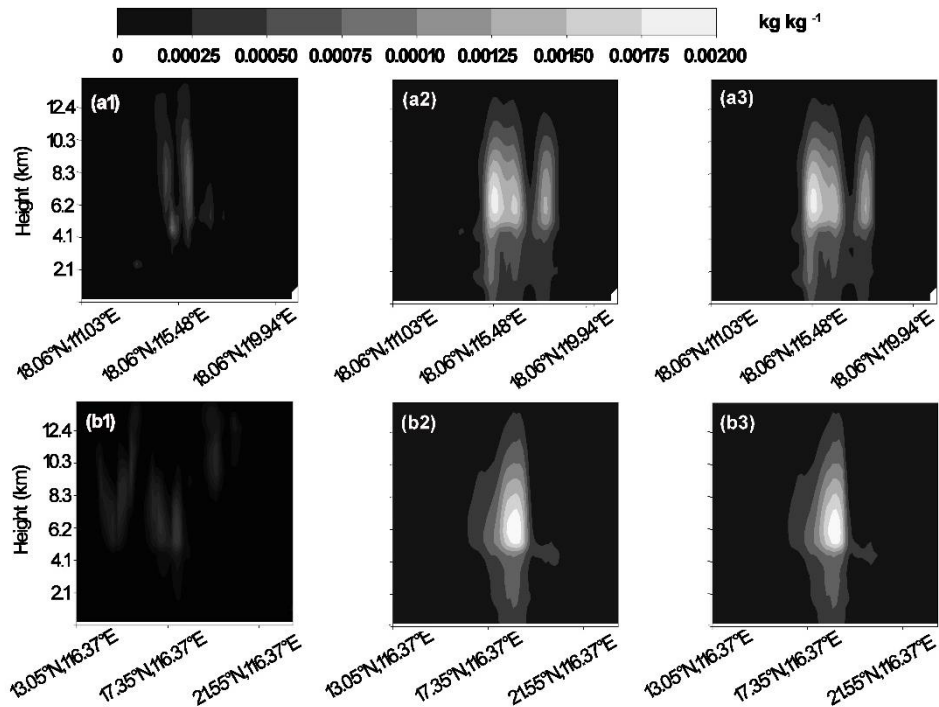
Figure 8. The x-press cross section of cloud water and ice mixing ratio for Exp-01 at 02:00 UTC, 18 August, 2020 for the AB (the
440 **upper panel) and CD (the lower panel) lines shown by Figure 1. From left to right, the column panels correspond to the nature run, the first guess and the analysis estimates.**

Assimilating VIS radiance data does not improve the underprediction in vertical and horizontal firections. In the vertical direction, a one-layer cloud was reported between 4 ~ 12 km height for the nature run (Figure 8(a1) and 8(b1)). However, clouds were presented between 0 ~ 12 km height for the prior estimate (Figure 8(a2) and 8(b2)). After the assimilation, the
445 updated atmosphere state suggested decreased Qc/Qi, but clouds below 4 km height were not removed (Figure 8(a3) ~ 8(b3)). In the horizontal direction, a one-layer thin cloud was presented between 14 N ~ 16 N for the nature run (Figure 8 (b1)). Such cloud fragment was not simulated for the prior estimate of atmosphere state (Figure 8 (b2)), nor was it regenerated after assimilating the VIS radiance data (Figure 8(b3)). Namely, assimilating the VIS radiance data could not generate cloud hydrometers from clear sky as indicated by the prior estimate due to the zero spread of cloud variables.

450   Quantitative analyses of CWP and CFC indicated improved analysis and first-guess forecasts for the cycled DA experiments, with the influences varying with different parameters and model settings which will be discussed in the following sections.

a. Influences of filter algorithms

455   To see how different filters influence the analysis and first-guess forecast of cloud variables, quantitative analyses of FSS and MAE of the ensemble mean CWP for Exp-01 ~ Exp-03 (EAKF) and Exp-04 ~ Exp-06 (RHF) are presented in Figure 9. In general, the performance of RHF is comparable to or slightly better than EAKF. At some analysis times before 03:00 UTC, the posterior estimate of FSS is larger for Exp-01 than for Exp-04, but the first-guess FSS at the next analysis time is larger for Exp-04 than Exp-01. Similar results were found for the 1 hr and 3 hr first-guess forecasts. The results imply that better analyses do not always ensure better forecasts. The differences in the analysis and forecast between EAKF and
460 RHF are closely related to the posterior estimate of the cloud and non-cloud variables.
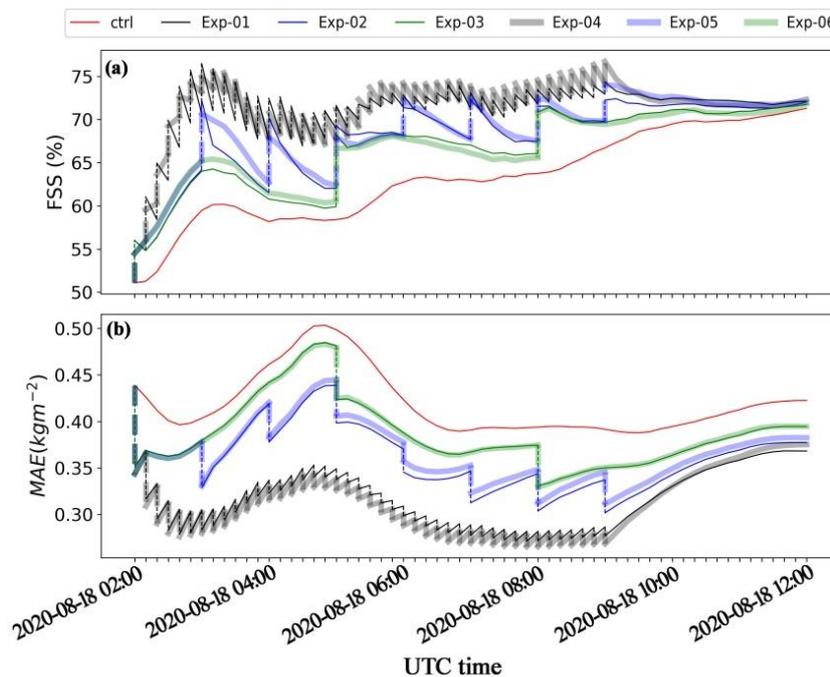
Figure 9. The time evolution of FSS and MAE for the ensemble mean first-guess forecast and analysis for the cycled DA experiments which are designed to illustrate the sensitivity to filter algorithms.

   EAKF assumes a Gaussian prior PDF. In comparison, RHF does not need Gaussian assumption. However, the
465 performance of RHF is subject to the sampling errors due to limited ensemble members and other factors as indicated by Anderson (2010). Therefore, only comparable or slightly better analysis and first-guess estimates were revealed for RHF than EAKF. In addition, updating the state variables by RHF is at a sacrifice of expensive computational cost. For the assimilation of 20567 observations in one assimilation cycle at a Linux cluster equipped with a 2.20 GHz Xeon Silver 4214 CPU with 12 cores, the elapsed CPU time is 775 s and 440 s for the RHF and EAKF methods, respectively.

 b. Influences of cycling variables

      The single observation experiments indicate that assimilating VIS radiance data generated neutral impacts on non-cloud variables at the first analysis time. However, it is not practical to exclude the non-cloud variables from the cycling variables in operational DA systems. To explore the impacts of including or excluding the updated non-cloud parameters to the next ensemble cycling, the 10 min and 1 hr first-guess forecast and analysis of FSS and MAE of the ensemble mean CWP for

475   Exp-01 ~ Exp-02 and Exp-07 ~ Exp-08 group are analysed. Figure 10 indicates that Exp-01 (Exp-02) outperforms Exp-07 (Exp-08). Namely, including the cloud and non-cloud variables in the ensemble cycling makes the forecasting more skillful than including the cloud variables alone. The results imply that beneficial impacts were introduced to the non-cloud variables, or at least part of the non-cloud variables, with model integration.
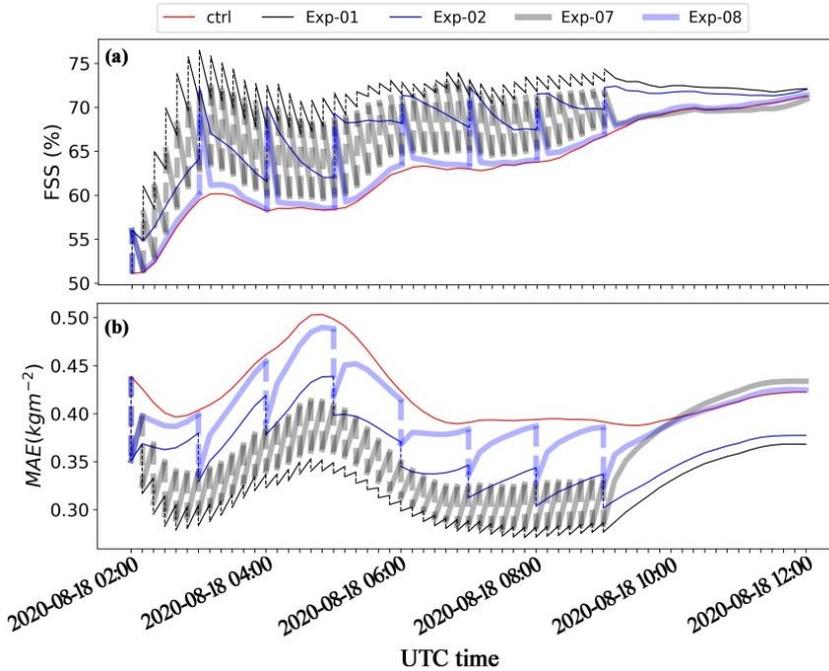
480   **Figure 10. The time evolution of FSS and MAE for the ensemble mean first-guess forecast and analysis for the cycled DA experiments which are designed to illustrate the sensitivity to cycling variables.**

      To demonstrate the error growth for the non-cloud variables, the temporal evolution of the ratio of benefits ℶ, calculated by formula (15), is presented by Figure 11.

$$ℶ = N_{bet}/N_{eff} \tag{15}$$

485   where N_{bet} denotes the number of horizontal grid boxes with negative differences of MPE between the posterior and the prior estimates (refer to section 2.4 and Scheck et al., 2020), N_{eff} denotes the number of observations effectively assimilated by the DA system (see the next section).
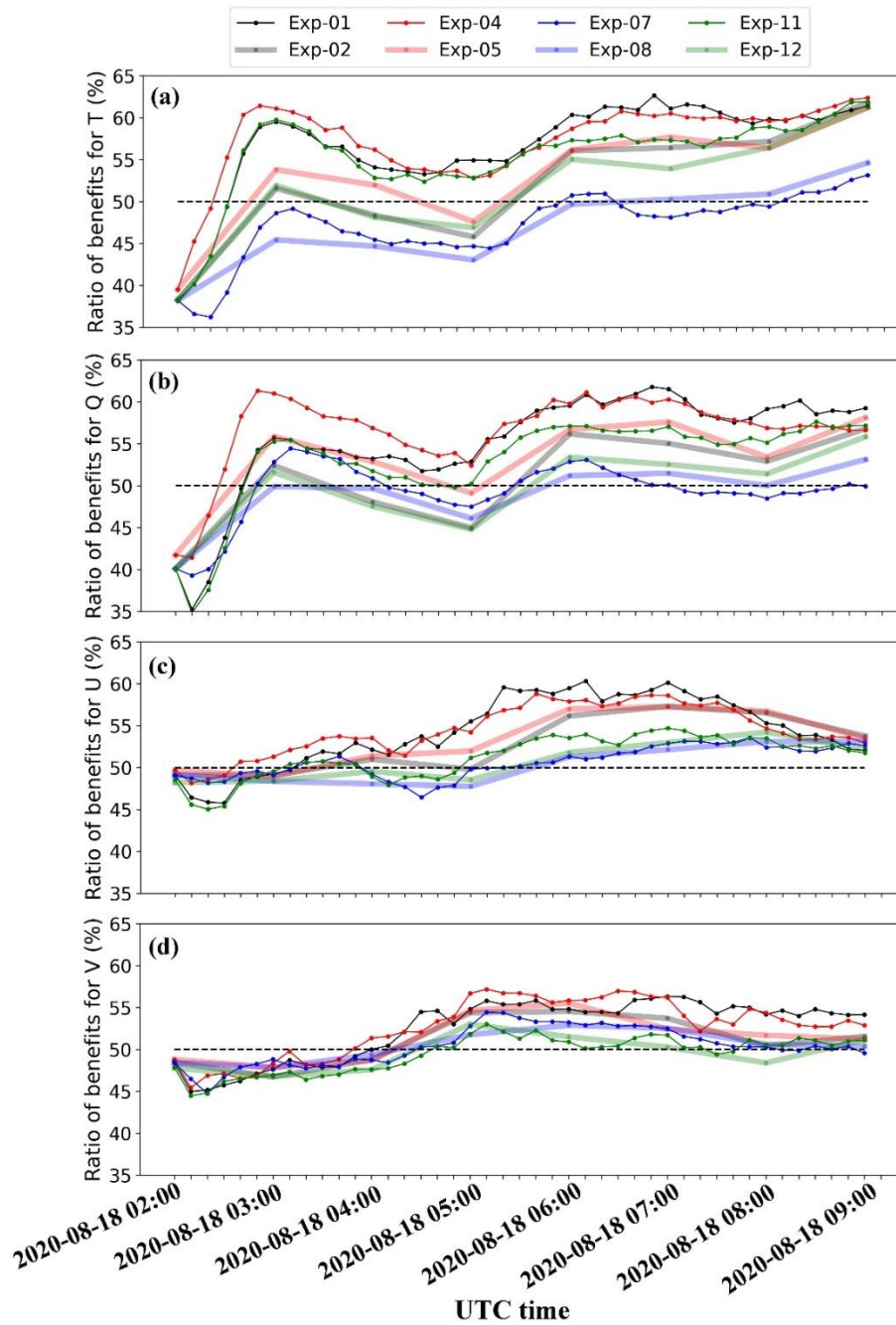
Figure 11. The time evolution of the ratio of beneficial impacts ⊃, calculated by formula (XXX) for (a), for first-guess forecast and analysis. The potential temperature (T); (b). Water vapour mixing ratio; (c). The x-wind component; (d). The y-wind component.

Figure 11 indicates positive impacts on the main non-cloud variables, especially at the later cycling steps. We think that a main reason is the positive feedback to the non-cloud variables due to the adjustment to cloud variables.

For the water vapour mixing ratio, if the prior ensemble mean equivalent radiance is overestimated compared with the observation, Qi/Qc tends to be decreased for the posterior estimate in order to generate a negative analysis increment in the observation space. In the next ensemble forecast cycle, the grid boxes with decreased Qi/Qc tend to generate hydrometeors due to condensation and freezing. This is because the surrounding atmosphere, which is supportive of more cloud hydrometeors, becomes over-saturated due to the loss of some cloud hydrometeors. The condensation and freezing are at a sacrifice of water vapour mixing ratio. As a result, the deceased Qi/Qc corresponds to the decreased water vapour mixing ratio. Accordingly, the VIS radiance could be positively related to the water vapour mixing ratio, and vice versa. According to formula (4), the covariance in observation space and state variable space will adjust the water vapour mixing ratio correctly.

The adjustment of temperature is more likely related to the interactions between clouds and radiation. For example, decreased CWP or CFC tends to enhance the direct radiation flux on the surface layer, increasing the low-level temperature toward the truth as indicated by Scheck et al. (2020), and vice versa. In addition, the interactions between clouds and longwave radiation tend to generate cooling effects at cloud top and heating effects at cloud bottom (Zhang et al., 2020). Therefore, a relationship between radiance (cloud) and temperature is expected, and the covariance in observation space and state variable space could adjust temperature correctly.

The impacts on the x- and y-wind components are slightly negative before 04:00 UTC, and become positive after that time. We think that the positive impacts are mainly caused by the convergence and divergence related to the thermal instability, which is closely related to cloud formation (increased radiance) and dissipation (decreased radiance) for convective weather systems. As indicated above, the cloud-radiation interactions tend to modify the temperature profile, which could strengthen or weaken the thermal instability and impact the z-wind component. The z-wind component is closely related to horizontal x- and y-wind components by adjusting the convergence and divergence (White et al., 2018). Therefore, an indirect "radiance——cloud——vertical velocity——convergence and divergence——horizontal wind" relationship could map the observation increment to the U and V increments correctly.

c. Influences of outlier threshold values

Not all observations were effectively assimilated by the WRF/DART-RTTOV system. Some of the observations were rejected by the DA system due to two reasons. 1) Non-monotonic pressure, i.e., pressure increases with altitude, was generated at some points during the interpolation of the perturbed first-guess model state to the RTTOV pre-defined layers. For the case study, non-monotonic pressure was mainly located in the Qinghai-Tibet Plateau, Tianshan Mountain, and Central Taiwan ranges (not shown for simplicity), where complex terrain exists. The results indicate that the performance of the WRF/DART-RTTOV system is slightly prohibited over complex terrain regions. 2) The differences between the observations and the prior ensemble mean equivalent observations are so large that these observations were rejected by the DA system because assimilating these data may cause the collapse of WRF model. For the observations rejected due to the second reason, the ratio of observations which could be effectively assimilated is dominated by the outlier threshold value. Increasing the outlier threshold value could increase the observation utilization (Figure 12), but it may introduce unstable

adjustments to state variables and may destroy the forecast. Therefore, a balance should be maintained between large outlier threshold value and the potentially detrimental effects on forecasts. The analysis and 10 min, 1 hr, and 3 hr first-guess forecasts indicate improved results for larger outlier threshold value (Figure 13). The case study indicates that setting the outlier threshold value to 6 does not cause the collapse of WRF, but generates improvements to the analysis and first-guess forecasts of CWP and cloud coverage.
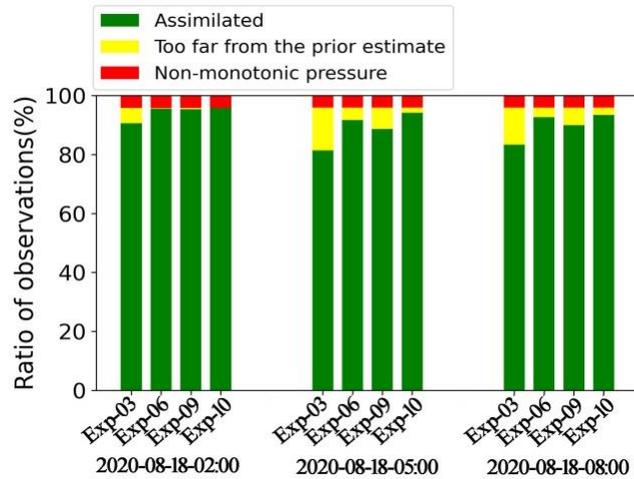
Figure 12. The ratio of observations assimilated or rejected by the WRF/DART system for different experiment designs.
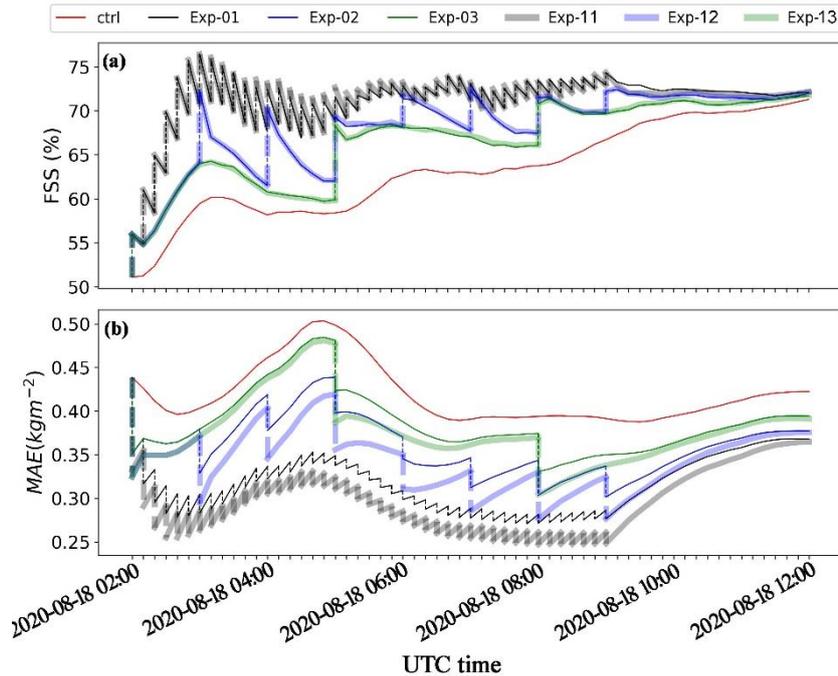
Figure 13. The time evolution of FSS and MAE for the ensemble mean first-guess forecast and analysis for the cycled DA experiments which are designed to illustrate the sensitivity to the outlier threshold values.

d. Influences of observation errors and thinning

The observation utilization is also influenced by the observation errors. Large observation errors correspond to large observation utilization (Figure 12). However, increasing observation errors implies less weight attached to the observations during the assimilation. Therefore, the analysis and first-guess forecast should be also influenced by the observation errors. To see how exactly the influences on the analysis and the first-guess forecasts, FSS and MAE of the ensemble mean CWP for the cycled DA experiments are presented in Figure 14. The analysis and first-guess forecasts of CWP and cloud coverage are negatively related to the observation errors. As complementary to the parameters controlling the number of observations, the influences of Exp-14 with thinned observations assimilated were presented. The results indicate only slight improvements to the first-guess forecast and analysis.
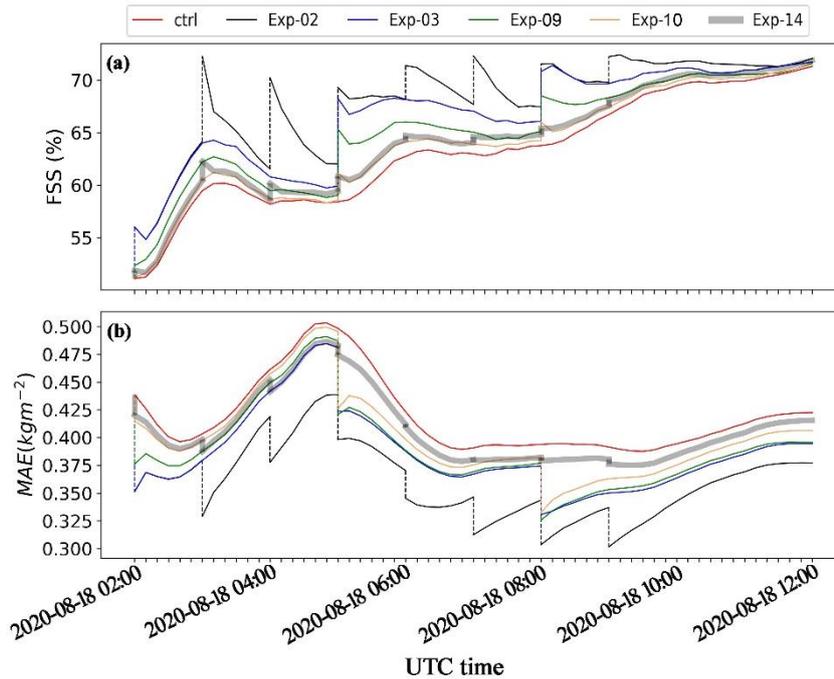
Figure 14. The time evolution of FSS and MAE for the ensemble mean first-guess forecast and analysis for the cycled DA experiments which are designed to illustrate the sensitivity to the observation errors.

3.2.2 Impacts on precipitation

The first-guess forecasts of rain rate for the nature run, control run, Exp-01, and Exp-11 are shown in Figure 15. On the domain average, rain rate was overestimated for the control and cycled DA experiments. Compared with the control run, precipitation was decreased in most cases for the cycled DA experiments, and the areas with or without precipitation are in better agreement with the nature run (Figure 16(a)).
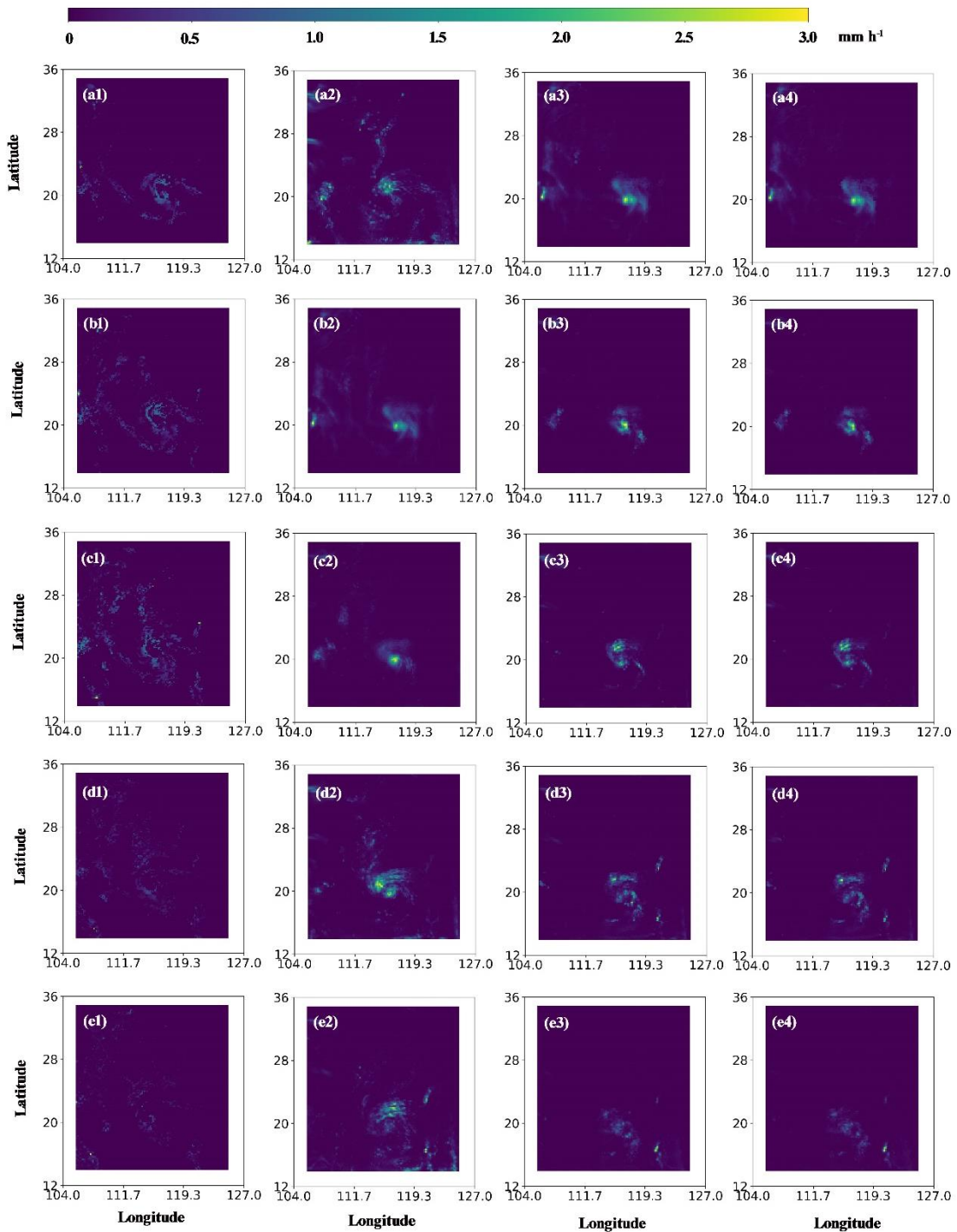
555 **Figure 15. The time evolution of rain rate for the nature run (column 1), the control run (column 2), the first-guess forecast of Exp-01 (column 3) and Exp-11(column 4). From top to bottom, the row panels correspond to the results for 02:00~02:10, 04:00~04:10, 06:00~06:10, 08:00~08:10, and 10:00~10:10 UTC 18 August, 2020.**

Quantitative metrics of rain rate forecast indicate that the forecasting skills were improved at most of the analysis times (Figure 16(b)). However, the improvements on rain rate were not expected at any time. For example, at the initial cycling

560 step (before 04:00 UTC, August 18, 2020), the control run seems to outperform other cycled DA experiments. With model integration, the advantages of assimilating VIS radiance data became apparent. The improved TS score was closely related to the improved CWP and cloud coverage simulations. In contrast, the improvements on rain rate were not as apparent as CWP. Existing studies indicate that precipitation was closely related to cloud vertical structure (Kubar and Hartmann, 2008; Yan et al., 2019), the presence and distribution of liquid and ice hydrometeors (Field and Heymsfield, 2015; Mülmenstädt et al.,

565 2015; Korolev et al., 2017), surrounding atmosphere and dynamic state variables (Kanji et al., 2017), etc. Therefore, the limited effects on rain rate are subject to the inability of assimilating visible radiance data to constrain cloud vertical structures, to improve cloud phase simulations, and to correct cloud location errors with underprediction due to zero-spread problem, etc.

570
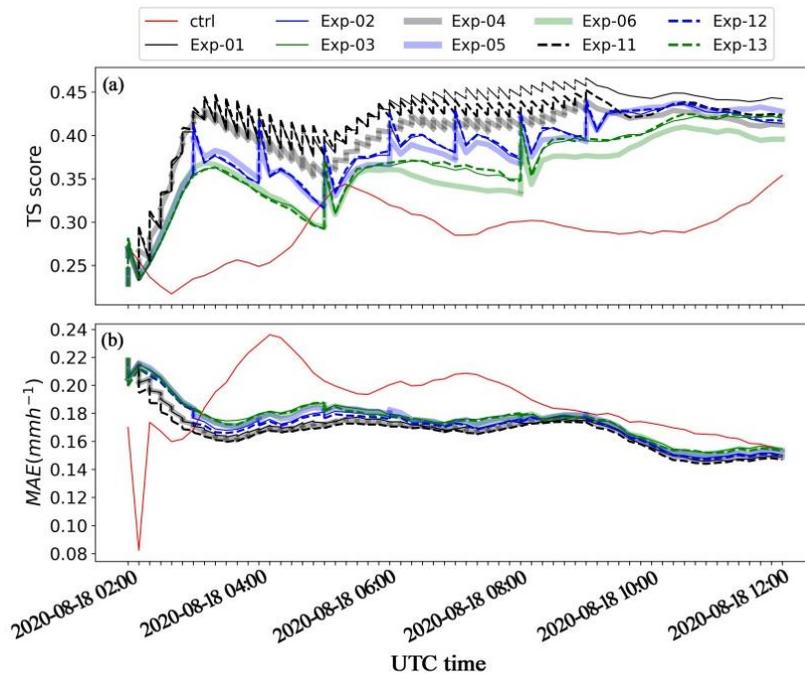
Figure 16. Quantitative metrics of rain rate for the first-guess forecast. (a). The Threat Score calculated by formula (10); (b). The mean absolute error (MAE) calculated by formula (8).

4. Discussion and Conclusions

575 In this study, single observation experiments and cycled DA experiments were performed in an OSSE framework to investigate the ability of the WRF/DART-RTTOV system for assimilating the simulated FY-4A/AGRI VIS (channel 2)

radiance at 15 km-resolution modelling. Single observation experiments were designed to reveal the abilities and inabilities of assimilating satellite VIS radiance data to cloud variables (liquid/ice water mixing ratio and CWP, effective radius of liquid water droplets, and cloud fraction) and non-cloud variables (water vapour mixing ratio, perturbation potential temperature, and wind). The cycled DA experiments were designed to explore the impacts of assimilating VIS radiance data on the analysis and first-guess forecasts of a tropical storm case with different model settings and observation preparations, including filter algorithms, cycling variables, updating frequencies, outlier threshold values, observation errors, and observations with or without thinning. General findings and discussions were provided below.

Single observation experiments in the first DA cycle indicate that assimilating the satellite VIS radiance data generated positive effects on cloud variables in most cases. In some rare cases, the assimilation increased the errors for the posterior estimate compared with the prior estimate both in the observation space or/and in the cloud variable (or diagnosed parameter CWP) space. These negative impacts were closely related to the non-linear properties of the forward operator and the non-Gaussian properties of the prior probability distribution function estimated from the limited prior ensemble members. In addition, neutral impacts were revealed on non-cloud variables including water vapour mixing ratio, temperature, and horizontal winds.

Although neutral impacts were revealed for the non-cloud parameters in the first DA cycle, including the non-cloud variables and cloud variables collectively in the next ensemble forecast cycle improved the first-guess forecast and analysis of cloud and non-cloud variables. The beneficial impacts of non-cloud variables are closely related to the feedback to the filtering adjustments to cloud variables by evaporation, condensation, freezing, and cloud-radiation interactions. Comparison between EAKF and RHF indicates slight advantages of RHF in dealing with non-Gaussian problems but at a sacrifice of around 1.8 times of more computational cost. In addition, the cycled DA experiments reveal that the first-guess and analysis results are positively related to the outlier threshold value and the updating frequency, and are negatively related to the observation errors and thinning length scale. Similar results were revealed for precipitation. The improvements were much more distinct for the representation of locations with or without precipitation than for the quantitative metrics of rain rate. The limited impacts of assimilating VIS radiance data on rain rate are subject to the inabilities to constrain cloud vertical structures, to improve cloud phase simulations, and to correct cloud location errors with underprediction due to zero-spread problem, etc.

The findings will provide some guidance on WRF/DART configurations and observation preparations in real DA application of FY-4A and the upcoming FY-4B VIS radiance data. The study is a supplement and an extent to a previous study by Scheck et al. (2020), which thoroughly discussed the potentials and limitations of assimilating the Meteosat SEVERI VIS imagery by the COSMO/KENDA system based on LETKF. In general, the pros and cons of assimilating the VIS radiance data in this study are in good agreement with Scheck et al. (2020), except that slight positive impacts on horizontal wind speeds were demonstrated in this study but Scheck et al. (2020) reported neutral impacts. We ascribe the slightly positive impacts on horizontal winds to the feedback to the convergence or divergence related to the "radiance——cloud——vertical velocity——convergence and divergence——horizontal winds" relationship. This relationship should

differ in weather systems. Therefore, the different impacts on horizontal wind speeds revealed by the two studies could be caused by differences in the weather systems. In addition, the two studies differ in the models/tools and corresponding configurations. This study explored some properties unique to the WRF/DART system. Besides the EAKF method, the non-Gaussian method RHF was also discussed in assimilating the VIS radiance data in this study. The advantages of RHF in dealing with non-Gaussian problems and its limitation in computation efficiency were discussed.

Nevertheless, this study only discussed low-resolution model simulations (15 km × 15 km). The grid spacing of 15 km is large enough to avoid radiance simulation errors due to 3D radiative effects, which are apparent for high-resolution simulations (Várnai and Marshak, 2001). Although the 3D radiative transfer effects could be properly corrected by some of the forward operators incorporated into RTTOV, the related parameters and datasets specific to FY-4A/AGRI are currently unavailable. Further studies should be extended to cloud-resolving model simulations like Scheck et al. (2020) to fully take the advantage of high-resolution satellite VIS radiance data, but attention should be paid to the forward operator because the enhanced 3D radiative effects for high-resolution modelling could make the nonlinearity of forward operator more complicated. An outlook of future work should also include the following aspects.

(1) Optimization of forward operators and estimation of observation errors. The findings in this study suggest that observation errors should be as small as possible to improve the first-guess forecast and analysis. One of the factors determining the observation error is the forward operator (Janjić et al., 2017). Therefore, it is necessary to optimize the RTTOV configurations in simulating synthetic FY-4A visible imagery from WRF model state variables and to give an estimate of observation errors under different modelling resolutions, weather conditions, sun-viewing geometries, etc. Scheck et al. (2018) assessed the performance of the forward operator MFASIS by comparing the synthetic visible imagery simulated based on the state variables from COSMO with the SEVIRI visible image. Perhaps their work could be referenced to assess the performance of WRF-RTTOV systems against FY-4A visible observations.

(2) Improvements on computational cost and accuracy of forward operators. Assimilating the visible radiance data is quite time-consuming for the current WRF/DART-RTTOV system (around 7 min in an EAKF cycle and 13 min in a RHF cycle). Increasing the updating frequency and outlier threshold value makes the computational cost more expensive. Currently, an accurate and fast observation operator for assimilating the FY-4A (and the upcoming FY-4B) visible radiance data at both low- and high-resolution simulations are still in need. Scheck et al. (2016a, 2021) developed a Look-up Table (LUT)- and machine learning-based forward operator, which is several orders faster than DOM-based methods. In addition, three-dimensional radiative effects could be corrected for high-resolution modelling without too expensive computation cost (Scheck et al., 2018; Albers et al., 2020; Zhou et al., 2021). These methods could benefit to improve forward operators.

(3) Correction of errors due to non-Gaussian and non-linear problems. The performance of EAKF was limited to the non-linear and non-Gaussian problems. The Particle Filter (PF) is declared to have advantages in dealing with the non-Gaussian and non-linear problems. With certain localized method included, PF shows great potential in application to high-dimension numerical prediction model such as the WRF model (Shen and Tang, 2015; Poterjoy, 2016; Pinheiro et al., 2019).

Therefore, newly-developed PF methods could be a candidate to further improve the forecasting skills of WRF model when
645 satellite visible radiance data are assimilated.

(4) Techniques to reduce the cloud location errors. The performance of WRF/DART system is limited to location errors, especially in the case where the first guess indicates underpredicted clouds. Dowell et al. (2012) promoted a method to tackle the location errors in assimilating radar data by EnKF. Their basic idea was to add perturbations to the base state randomly and add local perturbations in and near precipitation areas regularly to produce clouds in precipitation areas. In addition,
650 White et al. (2018) also promoted a method to produce clouds comparable to satellite observations, but this method needs other observations (such as brightness temperature at infrared bands). These methods are potentially useful to correct the location errors due to the zero spread of prior ensemble members in the satellite VIS radiance DA.

Code and data availability

Version 4.1.1 of WRF-ARW source code is publicly available at http://www2.mmm.ucar.edu/wrf/users/. The Manhattan release
655 of DART source code (version 9.8.0), including the RTTOV observation operator (version 12.3), is publicly available at https://dart.ucar.edu/. Version 12.3 of RTTOV source code is publicly available at https://nwp-saf.eumetsat.int/site/software/rttov/. The NCEP FNL (Final) Operational Global Analysis data are downloaded from https://rda.ucar.edu/datasets/ds083.2/. The ERA5 hourly data are available at https://cds.climate.copernicus.eu/api/v2/resources. The source codes of WRF-ARW, WPS, RTTOV, and DART models
660 (tool), as well as the input and (processed) output data, and the visualization scripts are available at https://zenodo.org/record/6898477#.YuB9c4RBzD4.

Author contribution

Yongbo Zhou: Conceptualization, Methodology, Writing original draft, Visualization, Funding acquisition. Yubao Liu: Conceptualization, review and editing. Zhaoyang Huo, review and editing. Yang Li, review and editing.

Competing interests
665

The authors declare that they have no conflict of interest.

Acknowledgement

This study is supported by the Natural Science Foundation of Jiangsu Province (Grant No. BK0210665) and Startup Foundation for Introducing Talent of Nanjing University of Information Science and Technology (Grant No. 2019r095). We
670 are grateful to Glen Romine, Moha Gharamti, Nancy Collins, and Tim Hoar from the DART team at the National Center for

Atmospheric Research for kindly providing instructions on running this tool. We acknowledge the High Performance Computing Center of Nanjing University of Information Science & Technology for their support of this work. We are grateful to the two anonymous reviewers for their constructive comments and suggestions.

References

675 Albers, S., Saleeby, M. S., Kreidenweis, S., Bian, Q., Xian, P., Toth, Z., Ahmadov, R., James, E., and Miller, D. S.: A fast visible-wavelength 3D radiative transfer model for numerical weather prediction visualization and forward modeling, Atmos. Meas. Tech., 13, 3235–3261, doi: 10.5194/amt-13-3235-2020, 2020.

Anderson, J. L.: An Ensemble Adjustment Kalman Filter for Data Assimilation, Mon. Weather Rev., 129, 2884-2903, doi:10.1175/1520-0493(2001)129<2884:AEAKFF>2.0.CO;2, 2001.

680 Anderson, J. L.: An adaptive covariance inflation error correction algorithm for ensemble filters, Tellus A, 59, 210-224, doi:10.1111/j.1600-0870.2006.00216.x, 2007.

Anderson, J. L.: Spatially and temporally varying adaptive covariance inflation for ensemble filters, Tellus A, 61, 72–83, doi:10.1111/j.1600-0870.2008.00361.x, 2009.

Anderson, J. L.: Localization and Sampling Error Correction in Ensemble Kalman Filter Data Assimilation, Mon. Wea. Rev., 685 140(7), 2359-2371, doi:10.1175/MWR-D-11-00013.1, 2012.

Anderson, J. L.: A Non-Gaussian Ensemble Filter Update for Data Assimilation, Mon. Wea. Rev., 138(11): 4186–4198, doi: 10.1175/2010MWR3253.1, 2010.

Anderson, J., Hoar, T., Raeder, K., Liu, H., Collins, N., Torn, R., and Avellano, A.: The Data Assimilation Research Testbed: A Community Facility, B. Am. Meteorol. Soc., 90(9), 1283-1296, doi:10.1175/2009BAMS2618.1, 2009.

690 Baren, A. J., Cotton, R., Furtado, K., Havemann, S., Labonnote, L.-C., Marenco, F., Smith, A., and Thelen. J.-C.: A self-consistent scatteringmodel for cirrus. II: The high and low frequencies, Q. J. R. Meteorol. Soc., 140: 1039-1057, doi:10.1002/qj.2193, 2014.

Bauer, P., Geer, J. A., Lopez, P., and Salmond, D.: Direct 4D-Var assimilation of all-sky radiances. Part I: Implementation, Q. J. R. Meteorol. Soc., 136(152): 1868-1885, doi: 10.1002/qj.659, 2010.

695 Bauer, P., Ohring, G., Kummerow, C., and Auligne, T.: Assimilating satellite observations of clouds and precipitation into NWP models, B. Am. Meteorol. Soc., 92, ES25-ES28, doi:10.1175/2011BAMS3182.1, 2011.

Bretherton, C. S., and Park, S.: A New Moist Turbulence Parameterization in the Community Atmosphere Model, J. Clim., 22, 3422-3448, doi: 10.1175/2008JCLI2556.1, 2009.

Buehner, M., Houtekamer, P. L., Charette, C., Mitchell, H. L., and He, B.: Intercomparison of Variational Data Assimilation 700 and the Ensemble Kalman Filter for Global Deterministic NWP. Part I: Description and Single-Observation Experiments, Mon. Wea. Rev., 138(5): 1550-1566, doi: 10.1175/2009MWR3157.1, 2013.

Carminati, F. , and Migliorini, S.: All-sky Data Assimilation of MWTS-2 and MWHS-2 in the Met Office Global NWP System, Adv. Atmos. Sci., 38: 1682-1694, doi: 10.1007/s00376-021-1071-5, 2021.

Coste, P., Pasternak, F., Faure, F., Jacquet, B., Bianchi, S., Aminou, D. M. A., Luhmann, H. J., Hanson, C., Pili, P., and Fowler, G.: SEVIRI, the imaging radiometer on Meteosat second generation: in-orbit results and first assessment, Proceedings of the SPIE, 10568, 105680L, doi:10.1117/12.2308023, 2017.

Di, Z., Gong, W., Gan, Y., Shen, C., and Duan, Q.: Combinatorial Optimization for WRF Physical Parameterization Schemes: A Case Study of Three-Day Typhoon Simulations over the Northwest Pacific Ocean, Atmosphere, 10(5), 233; doi: 10.3390/atmos10050233, 2019.

Dowell, D. C., Wicker, L. J., and Snyder, C.: Ensemble Kalman Filter Assimilation of Radar Observations of the 8 May 2003 Oklahoma City Supercell: Influences of Reflectivity Observations on Storm-Scale Analyses, Mon. Wea. Rev., 139(1): 272-294, doi: 10.1175/2010MWR3438.1

Dudhia, J.: A Multi-layer Soil Temperature Model for MM5, Preprints, Sixth PSU/NCAR Mesoscale Model Users' Workshop, Boulder, 22-24 July 1996, pp. 49-50

Field, P. R., and Heymsfield, A. J.: Importance of snow to global precipitation, Geophys. Res. Lett., 42, 9512-9520, doi: 10.1002/2015GL065497, 2015.

Gao, J. D., Xue, M., and Stensrud, D. J.: The Development of a Hybrid EnKF-3DVAR Algorithm for Storm-Scale Data Assimilation, Adv. Meteorol., 2013, 512656, doi: 10.1155/2013/512656, 2013.

Geer, A. J., Bauer, P., and O'Dell, C. W.: A revised cloud overlap scheme for fast microwave radiative transfer in rain and cloud, J. Appl. Meteorol. Clim., 48, 2257–2270, doi: 10.1175/2009JAMC2170.1, 2009.

Geer, A. J., Lonitz, K., Weston, P., Kazumori, M., Okamoto, K., Zhu, Y., Liu, H. E., Collard, A., Bell, W., Migliorini, S., Chambon, P., Fourrié, N., Kim, M.-J., Köpken-Watts, C., and Schraff, C.: All-sky satellite data assimilation at operational weather forecasting centres, Q. J. R. Meteorol. Soc., 144(713): 1191-1217, doi: 10.1002/qj.3202, 2017.

Geer, A. J., Migliorini, S., and Matricardi, M.: All-sky assimilation of infrared radiances sensitive to mid- and upper-tropospheric moisture and cloud, Atmos. Meas. Tech., 12, 4903-4929, doi:10.5194/amt-12-4903-2019, 2019.

Hasselmann, K., Barnett, T. P., Bouws, E., Carlson, H., Cartwright, D. E., Enke, K., Ewing, J. A., Gienapp, H., Hasselmann, D. E., Kruseman, P., Meerburg, A., Müller, P., Olbers, D. J., Richter, K., Sell, W., and Walden, H.: Measurements of wind-wave growth and swell during the Joint North Sea Wave Project (JONSWAP), Deutches Hydrographisches Institut, 12, 95 pp., http://resolver.tudelft.nl/uuid:f204e188-13b9-49d8-a6dc-4fb7c20562fc, 1973.

Hu, J., Fu, Y., Zhang, P., Min, Q., Gao, Z., Wu, S., and Li, R.: Satellite Retrieval of Microwave Land Surface Emissivity under Clear and Cloudy Skies in China Using Observations from AMSR-E and MODIS, Remote Sens., 13(19), 3980, doi: 10.3390/rs13193980, 2021.

Iacono, M. J., Delamere, J. S., Mlawer, E. J., Shephard, M. W., Clough, S. A., and Collins, W. D.: Radiative forcing by long-lived greenhouse gases: Calculations with the AER radiative transfer models, J. Geophys. Res., 113, D13103, doi:10.1029/2008JD009944, 2008.

Janjić, T., Bormann, N., Bocquet, M., Carton, J. A., Cohn, S. E., Dance, S. L., Losa, S. N., Nichols, N. K., Potthast, R., Waller, J. A., Weston P., On the representation error in data assimilation, Q. J. R. Meteorol. Soc.,144(713): 1257-1278, doi: 10.1002/qj.3130, 2017

Jiménez, A., P., Dudhia, J., González-Rouco, J. F., Navarro, J., Montávez, P. J., and García-Bustamante, E.: A Revised Scheme for the WRF Surface Layer Formulation, Mon. Wea. Rev., 140(3): 898–918, doi: 10.1175/MWR-D-11-00056.1, 2012.

Kanji, A. J., Ladino, L. A., Wex, H., Boose, Y., Burkert-Hohn, M., Cziczo, D. J., and Krämer, M.:Overview of Ice Nucleating Particles, Meteor. Monographs, 58(1), 1.1–1.33, doi: 10.1175/AMSMONOGRAPHS-D-16-0006.1, 2017

Keat, W. J., Stein, T. H. M., Phaduli, E., Landman, S., Becker, E., Bopape, M.-J. M., Hanley, K. E., Lean, H. W., and Webster, S.: Convective initiation and stormlife cycles in convection-permitting simulations of the Met Office Unified Model over South Africa, Q. J. R. Meteorol. Soc., 145, 1323-1336, doi:10.1002/qj.3487, 2019.

Kostka, P. M., Weissmann, M., Buras, R., Mayer, B., and Stiller, O.: Observation operator for visible and near-infrared satellite reflectances, J. Atmos. Ocean. Tech., 31(6), 1216-1233, doi:10.1175/JTECH-D-13-00116.1, 2014.

Kubar, L. T., and Hartmann, D. L.: Vertical structure of tropical oceanic convective clouds and its relation to precipitation, Geophys. Res. Lett., 35, L03804, doi: 1029/2007GL032811, 2008.

Korolev, A., McFarquhar, G., Field, P. R., Franklin, C., Lawson, P., Wang, Z., Williams, E., Abel, S. J., Axisa, D., Borrmann, S., Crosier, J., Fugal, J., Krämer, M., Lohmann, U., Schlenczek, O., Schnaiter, M., and Wendisch, M.: Mixed-Phase Clouds: Progress and Challenges, Meteor. Monographs, 58(1), 5.1–5.50, doi: 10.1175/AMSMONOGRAPHS-D-17-0001.1, 2017.

Kurzrock, F., Nguyen, H., Sauer, J., Ming, F. C., Cros, S., Smith Jr. W. L., Minnis, P., Palikonda, R., Jones, T. A., Lallemand, C., Linguet, L., and Lajoie, G.: Evaluation of WRF-DART (ARW v3.9.1.1 and DART Manhattan release) multiphase cloud water path assimilation for short-term solar irradiance forecasting in a tropical environment, Geosci. Model Dev., 12, 3939-3954, doi:10.5194/gmd-12-3939-2019, 2019.

Lawson, W. G., and Hansen, J. A.: Implications of Stochastic and Deterministic Filters as Ensemble-Based Data Assimilation Methods in Varying Regimes of Error Growth, Mon. Wea. Rev., 132 (8), 1966–1981, doi: 10.1175/1520-0493(2004)132<1966:IOSADF>2.0.CO;2, 2004.

Lei, J., Bikel, P., and Snyder, C.: Comparison of Ensemble Kalman Filters under Non-Gaussianity, Mon. Wea. Rev., 138 (4): 1293–1306, doi: 10.1175/2009MWR3133.1, 2010.

Lei, L., Anderson, J. L., and Romine, G. S.: Empirical Localization Functions for Ensemble Kalman Filter Data Assimilation in Regions with and without Precipitation, Mon. Wea. Rev., 143(9), 3664-3679, doi:10.1175/MWR-D-14-00415.1, 2015.

Li, J., Geer, J. A., Okamoto, K., Otkin. A. J., Liu, Z., Han, W., and Wang, P.: Satellite All-sky Infrared Radiance Assimilation: Recent Progress and Future Perspectives, Adv. Atmos. Sci., 39(1): 9-21, doi: 10.1007/s00376-021-1088-9, 2022.

Ma, Z., Maddy, E. S., Zhang, B., Zhu, T., Boukabara, S. A.: Impact Assessment of Himawari-8 AHI Data Assimilation in NCEP GDAS/GFS with GSI, J. Atmos. Ocean. Tech., 34(4), 797-815, doi:10.1175/JTECH-D-16-0136.1, 2017.

Matricardi, M.: The generation of RTTOV regression coefficients for IASI and AIRS using a new profile training set and a new line-by-line database, ECMWF, Technical Memorandum, 564, 47 pp., https://doi.org/10.21957/59u3oc9es, 2008.

Mayer, B., and Kylling, A.: Technical note: The libRadtran software package for radiative transfer calculations—description and examples of use, Atmos. Chem. Phys., 5, 1855–1877,doi:10.5194/acp-5-1855-2005, 2005.

McCarty, W., Jedlovec, G., and Timothy L. M.: Impact of the assimilation of Atmospheric Infrared Sounder radiance measurements on short-term weather forecasts, J. Geophys. Res., 144, D18122, doi: 10.1029/2008JD011626, 2009.

Migliorini, S. and Candy, B.: All-sky satellite data assimilation of microwave temperature sounding channels at the Met Office, Q. J. R. Meteorol. Soc., 145(719), 867-883, doi:10.1002/qj.3470, 2019.

Mülmenstädt, J., Sourdeval, O., Delanoë, J., and Quaas, J.: Frequency of occurrence of rain from liquid-, mixed-, and ice-phase clouds derived from A-Train satellite retrievals, Geophys. Res. Lett., 42, 6502–6509, doi: 10.1002/2015GL064604, 2015.

Nakajima T., and King, M. D.: Determination of the optical thickness and effective particle radius of clouds from reflected solar radiation measurements. Part I: Theory, J. Atmos. Sci., 47(15): 1878-1893, doi:10.1175/1520-0469(1990)047<1878:DOTOTA>2.0.CO;2, 1990.

Pinheiro, F. R., van Leeuwen, P. J., and Geppert, G.: Efficient nonlinear data assimilation using synchronization in a particle filter, Q. J. R. Meteorol. Soc., 145:2510-2523, doi:10.1002/qj.3576.

Polkinghorne, R. and Vukicevic, T.: Data assimilation of cloud-affected radiances in a cloud-resolving model, Mon. Wea. Rev., 139(3), 755-773. doi:10.1175/2010MWR3360.1, 2011.

Poterjoy, J.: A Localized Particle Filter for High-Dimensional Nonlinear Systems, Mon. Wea. Rev., 144 (1), 59-76, doi: 10.1175/MWR-D-15-0163.1, 2016.

Prates, C., Migliorini, S., English, S., and Pavelinc, E.: Assimilation of satellite infrared sounding measurements in the presence of heterogeneous cloud fields, Q. J. R. Meteorol. Soc.,140: 2062-2077, doi: 10.1002/qj.2279, 2014.

Saunders, R., Hocking, J., Turner, E., Rayer, P., Rundle, D., Brunel, P., Vidot, J., Roquet, P., Matricardi, M., Geer, A., Bormann, N., and Lupu, C.: An update on the RTTOV fast radiative transfer model (currently at version 12). Geosci. Model Dev., 11(7), 2717-2737, doi:10.5194/gmd-11-2717-2018, 2018.

Scheck, L.: A neural network based forward operator for visible satellite images and its adjoint, J. Quant. Spectrosc. Radiat. Transf., 274, 107841, doi:10.1016/j.jqsrt.2021.107841, 2021.

Scheck, L., Frèrebeau, P., Buras-Schnell, R., and Mayer, B.: A fast radiative transfer method for the simulation of visible satellite imagery, J. Quant. Spectrosc. Radiat. Transf., 175, 54-67. doi:10.1016/j.jqsrt.2016.02.008, 2016a.

Scheck, L., Hocking, J., and Saunders, R.: A comparison of MFASIS and RTTOV-DOM. Report of Visiting Scientist mission NWP_VS16_01 (Document ID, NWPSAF-MO-VS-054), EUMETSAT. Retrieved from https://nwpsaf.eu/vs_reports/nwpsaf-mo-vs-054.pdf, 2016b.

Scheck, L., Weissmann, M., and Bernhard, M.: Efficient Methods to Account for Cloud-Top Inclination and Cloud Overlap in Synthetic Visible Satellite Images, J. Atmos. Ocean. Tech., 35, 665-685, doi:10.1175/JTECH-D-17-0057.1, 2018.

Scheck, L., Weissmann, M., and Bach, L.: Assimilating visible satellite images for convective-scale numerical weather prediction: A case-study, Q. J. R. Meteorol. Soc., 146(732), 3165-3186, doi:10.1002/qj.3840, 2020.

Schmit, T. J., Lindstrom, S. S., Gerth, J. J., and Gunshor, M. M.: Applications of the 16 spectral bands on the Advanced Baseline Imager (ABI), J. Operational Meteor., 6 (4), 33-46, doi:10.15191/nwajom.2018.0604, 2018.

Schröttle, J., Weissmann, M., Scheck, L., and Hutt, A.: Assimilating Visible and Infrared Radiances in Idealized Simulations of Deep Convection, Mon. Wea. Rev., 148(11), 4357-4375, doi:10.1175/MWR-D-20-0002.1, 2020.

Shen, F., Xu, D., Min, J., Chu, Z., and Li, X.: Assimilation of radar radial velocity data with the WRF hybrid 4DEnVar system for the prediction of hurricane Ike (2008), Atmos. Res., 234, 104771, doi: 10.1016/j.atmosres.2019.104771, 2020.

Shen, Z., and Tang, Y.: A modified ensemble Kalman particle filter for non-Gaussian systems with nonlinear measurement functions, J. Adv. Model. Earth Syst., 7, 50–66, doi:10.1002/2014MS000373, 2015.

Skamarock, W. C., Klemp, J. B., Dudhia, J., Gill, D. O., Barker, D. M., Duda, M. G., Wang, X.-Y., Wang, W., and Power, J. G.: A Description of the Advanced Research WRF Version 3 (No. NCAR/TN-475+STR), University Corporation for Atmospheric Research, doi:10.5065/D68S4MVH, 2008.

Stengel, M., Lindskog, M., Undén, P., and Gustafsson, N.: The impact of cloud-affected IR radiances on forecast accuracy of a limited-area NWP model, Q. J. R. Meteorol. Soc., 139(677): 2081-2096, doi: 10.1002/qj.2102, 2013.

Thompson, G., P. R. Field, R. M. Rasmussen, and W. D. Hall, 2008: Explicit forecasts of winter precipitation using an improved bulk microphysics scheme. Part II: implementation of a new snow parameterization, Mon. Wea. Rev., 136: 5095-5115, doi: 10.1175/1520-0493(2004)132<0519:EFOWPU>2.0.CO;2, 2008

Tiedtke, M.: A comprehensive mass flux scheme for cumulus parameterization in large-scale models, Mon. Wea. Rev., 117: 1779–1800, doi: 10.1175/1520-0493(1989)117<1779:ACMFSF>2.0.CO;2, 1989.

Vidot, J., and Borbás, É.: Land surface VIS/NIR BRDF atlas for RTTOV-11: model and validation against SEVIRI land SAF albedo product, Q. J. R. Meteorol. Soc., 140, 2186-2196, doi:10.1002/qj.2288, 2014.

Vidot, J., Brunel, P., Dumont, M., Carmagnola, C., and Hocking J.: The VIS/NIR Land and Snow BRDF Atlas for RTTOV: Comparison between MODIS MCD43C1 C5 and C6, Remote Sens., 10(1), 21, doi:10.3390/rs10010021, 2018.

Vukicevic, T., Greenwald, T., Zupanski, M., Zupanski, D., Vondar Harr, T., and Jones, A. S.: Mesoscale cloud state estimation from visible and infrared satellite radiance. Mon. Wea. Rev., 132(12): 3066-3077. doi:10.1175/MWR2837.1, 2004.

Várnai T. and Marshak A.: Statistical Analysis of the Uncertainties in Cloud Optical Depth Retrievals Caused by Three-Dimensional Radiative Effects, J. Atmos. Sci., 58(12), 1540-1548, doi:10.1175/1520-0469(2001)058<1540:SAOTUI>2.0.CO;2, 2001.

White, A. T., Pour-Biazar, A., Doty, K., Dornblaser, B., and McNider, R. T.: Improving Cloud Simulation for Air Quality Studies through Assimilation of Geostationary Satellite Observations in Retrospective Meteorological Modeling, Mon. Wea. Rev., 146(1): 29-48, doi: 10.1175/MWR-D-17-0139.1, 2018.

840 Xu, D., Min, J., Shen, F., Ban, J., and Chen, P.: Assimilation of MWHS radiance data from the FY-3B satellite with the WRF Hybrid-3DVAR system for the forecasting of binary typhoons, J. Adv. Model. Earch Syst., 8(2): 1014-1028, doi: 10.1002/2016MS000674, 2016.

Xu, K.-M., and Randall, A. D.: A Semiempirical Cloudiness Parameterization for Use in Climate Models, J. Atmos. Sci., 53(21): 3084–3102, doi: 10.1175/1520-0469(1996)053<3084:ASCPFU>2.0.CO;2, 1996.

845 Xue, J. S.: Scientific issues and perspective of assimilation of meteorological satellite data, Acta Meteorol. Sin., 67(9), 903-911, 2009, https://doi.org/10.3321/j.issn:0577-6619.2009.06.001, 2009 (in Chinese with English abstract).

Yan, Y., and Liu, Y.: Vertical Structures of Convective and Stratiform Clouds in Boreal Summer over the Tibetan Plateau and Its Neighboring Regions, Adv. Atmos. Sci., 36 (10), 1089−1102, doi: 10.1007/s00376-019-8229-4, 2019.

Yang, C., Liu, Z., Bresch, J., Rizvi, S. R. H., Huang, X.-Y., and Min, J.: AMSR2 all-sky radiance assimilation and its impact
850 on the analysis and forecast of Hurricane Sandy with a limited-area data assimilation system, Tellus A: Dynamic Meteorology and Oceanography, 68:1, 30917, doi: 10.3402/tellusa.v68.30917, 2016.

Yang, J., Zhang, Z., Wei, C., Lu, F., and Guo, Q.: Introducing the New Generation of Chinese Geostationary Weather Satellites, Fengyun-4, B. Am. Meteorol. Soc., 98(8), 1737-1658, doi:10.1175/BAMS-D-16-0065.1, 2017.

Zhang, A. and Fu. Y.: Life Cycle Effects on the Vertical Structure of Precipitation in East China Measured by Himawari-8
855 and GPM DPR, Mon. Wea. Rev., 146(7), 2183–2199, doi:10.1175/MWR-D-18-0085.1, 2018.

Zhang, C., Wang, Y. and Hamilton, K.: Improved Representation of Boundary Layer Clouds over the Southeast Pacific in ARW-WRF Using a Modified Tiedtke Cumulus Parameterization Scheme, Mon. Wea. Rev., 139(11): 3489–3513, doi: 10.1175/MWR-D-10-05091.1, 2011.

Zhang, M., Zupanski, M., Kim, M.-J., and Knaff, J. A.: Assimilating AMSU-A Radiances in the TC Core Area with NOAA
860 Operational HWRF (2011) and a Hybrid Data Assimilation System: Danielle (2010), Mon. Wea. Rev., 141(11), 3889-2907, doi:10.1175/MWR-D-12-00340.1, 2013.

Zhang, P., Zhu, L., Tang, S., Gao, L., Chen, L., Zheng, W., Han, X., Chen, J., and Shao, J.: General Comparison of FY-4A/AGRI With Other GEO/LEO Instruments and Its Potential and Challenges in Non-meteorological Applications, Front. Earth Sci., 6, 224, doi:10.3389/feart.2018.00224, 2019.

865 Zhang, T., Sun, J., and Yang, L.: A Numerical Study of Effects of Radiation on Deep Convective Warm Based Cumulus Cloud Development with a 3-D Radiative Transfer Model, Atmosphere, 11(11), 1187, doi: 10.3390/atmos11111187, 2020.

Zhou, Y. B., Liu, Y. B., Huo, Z. Y., and Li, Y.: WRF-DART/RTTOV input and (processed) output files for GMD-2022-30, Zenodo, doi: 10.5281/zenodo.6898477, 2022.

870   Zhou, Y. B., Liu, Y. B., and Liu, C.: A machine learning-based method to account for 3D Short-Wave radiative effects in 1D satellite observation operators, J. Quant. Spectrosc. Radiat. Transf., 275, 107891, doi:10.1016/j.jqsrt.2021.107891, 2021.

Zhu, Y., Liu, E., Mahajan, R., Thomas, C., Groff, D., Van Delst, P., Collard, A., Treadon, R., and Derber, C. J.: All-Sky Microwave Radiance Assimilation in NCEP's GSI Analysis System, Mon. Wea. Rev., 144(12): 4709–4735, doi: 10.1175/MWR-D-15-0445.1, 2016.